The Mid-infrared Molecular Inventory toward Orion IRc2

Sarah Nickerson[1,2], Naseem Rangwala[3], Sean W. J. Colgan[1], Curtis DeWitt[4], Jose S. Monzon[5], Xinchuan Huang[1,6], Kinsuk Acharyya[7], Maria N. Drozdovskaya[8], Ryan C. Fortenberry[9], Eric Herbst[10], and Timothy J. Lee[1,11]

[1] Space Science and Astrobiology Division, NASA Ames Research Center, Moffett Field, CA, 94035 USA; sarah.nickerson@nasa.gov
[2] Bay Area Environmental Research Institute, Moffett Field, CA 94035, USA
[3] Science Directorate, NASA Ames Research Center, Moffett Field, CA 94035 USA
[4] USRA, SOFIA, NASA Ames Research Center MS 232-11, Moffett Field, CA, 94035, USA
[5] Department of Astronomy, Yale University, P.O. Box 208101, New Haven, CT 06520-8101, USA
[6] SETI Institute, 339 Bernardo Avenue, Suite 200, Mountain View, CA 94043 USA
[7] Planetary Science Division, Physical Research Laboratory, Ahmedabad, 380009, India
[8] Center for Space and Habitability, University of Bern, Gesellschaftsstrasse 6, CH-3012 Bern, Switzerland
[9] Department of Chemistry and Biochemistry, University of Mississippi, MS 38677 USA
[10] Departments of Chemistry and Astronomy, University of Virginia, McCormick Road, Charlottesville, VA 22904 USA

Abstract

We present the first high spectral resolution mid-infrared survey in the Orion BN/KL region, covering 7.2–28.3 μm. With SOFIA/EXES, we target the enigmatic source Orion IRc2. While this is in the most prolifically studied massive star-forming region, longer wavelengths and molecular emission lines dominated previous spectral surveys. The mid-infrared observations in this work access different components and molecular species in unprecedented detail. We unambiguously identify two new kinematic components, both chemically rich with multiple molecular absorption lines. The "blue clump" has $v_{\rm LSR} = -7.1 \pm 0.7$ km s^{-1}, and the "red clump" has 1.4 ± 0.5 km s^{-1}. While the blue and red clumps have similar temperatures and line widths, molecular species in the blue clump have higher column densities. They are both likely linked to pure rotational H$_2$ emission also covered by this survey. This work provides evidence for the scenario that the blue and red clumps are distinct components unrelated to the classic components in the Orion BN/KL region. Comparison to spectroscopic surveys toward other infrared targets in the region show that the blue clump is clearly extended. We analyze, compare, and present in-depth findings on the physical conditions of C$_2$H$_2$, ^{13}CCH$_2$, CH$_4$, CS, H$_2$O, HCN, H^{13}CN, HNC, NH$_3$, and SO$_2$ absorption lines and an H$_2$ emission line associated with the blue and red clumps. We also provide limited analysis of H$_2$O and SiO molecular emission lines toward Orion IRc2 and the atomic forbidden transitions [Fe II], [S I], [S III], and [Ne II].

Unified Astronomy Thesaurus concepts: Infrared astronomy (786); Interstellar medium (847); Molecular spectroscopy (2095); Spectral line identification (2073); Molecular physics (2058); Astrochemistry (75); Star forming regions (1565); Star formation (1569); Interstellar line absorption (843); Interstellar line emission (844); Astrophysical processes (104); Atomic spectroscopy (2099)

Supporting material: machine-readable table

1. Introduction

The closest and best-studied massive star-forming region is the Orion Molecular Cloud 1 (OMC-1; Genzel & Stutzki 1989) with a distance of 418 ± 6 pc (Kim et al. 2008). The Becklin–Neugebauer/Kleinmann-Low region (Orion BN/KL; Becklin & Neugebauer 1967; Kleinmann & Low 1967) within OMC-1 has been the subject of numerous molecular emission line surveys across several decades, ranging from the far-infrared (FIR) to radio spectroscopy (e.g., Johansson et al. 1984; Blake et al. 1987; Sutton et al. 1995; Schilke et al. 1997, 2001; Comito et al. 2005; Lerate et al. 2006; Olofsson et al. 2007; Tercero et al. 2010; Crockett et al. 2014; Feng et al. 2016; Gong et al. 2015; Rizzo et al. 2017; Luo et al. 2019; Peng et al. 2019; refer to Gong et al. 2015 for a more complete list).

The emission lines in these previous FIR to radio surveys are typically divided into four classic components that each have distinct central velocities and line widths. The extended ridge is the quiescent, ambient gas of the molecular cloud. The compact ridge is a smaller region of denser, hotter quiescent gas separate from the extended ridge. The plateau is an outflow of shocked gas that may be further subdivided into a high- and a low-velocity flow. Finally, the hot core is the hot, dense gas rich in molecular species (Blake et al. 1987; Genzel & Stutzki 1989).

Figure 1 provides an overview of the Orion BN/KL region, indicating objects discussed in the following paragraphs and throughout this work. The region's complex morphology may be due to a recent explosive event. About 500 yr ago, a multibody encounter between the massive protostars radio source I, BN, and source n ejected the three objects and launched a massive outflow of gas from the Orion BN/KL region (Bally et al. 2011, 2015, 2017). Source I is a heavily embedded protostar candidate with no infrared counterpart (Churchwell et al. 1987; Greenhill et al. 2004) that drives regional outflows and masers (Menten & Reid 1995; Greenhill et al. 1998; Plambeck et al. 2009; Hirota et al. 2017; Wright et al. 2020, 2022).

Concurrent with sources I and n lies the Orion hot core. Despite being the first discovered and eponymous hot core (Ho et al. 1979), the nature of the hot core is atypical. Hot cores are
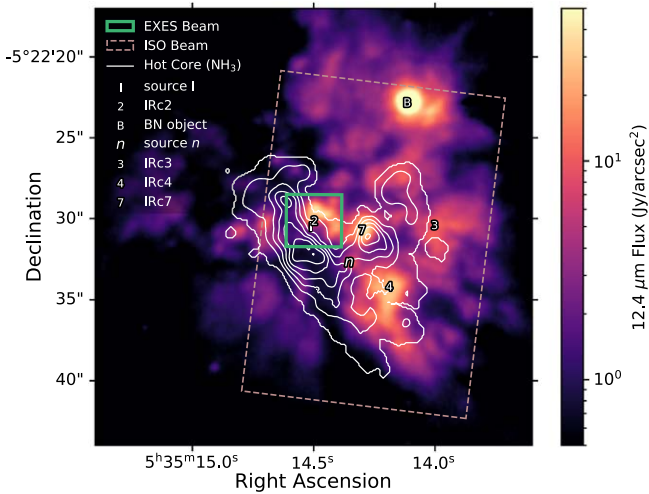

Figure 1. Mid-infrared (MIR) image of the BN/KL region. The color map is the 12.4 μm flux (SUBARU/COMICS; Okumura et al. 2011). White contours are the hot core traced by the NH$_3$ inversion transition (J, K) = (7, 7) (NRAO/EVLA; Goddi et al. 2011), and each level is 75 mJy beam^{-1} km s^{-1}. The thick green box is the EXES beam for the 7.6a μm setting. The dashed brown box is the smallest beam used in the Infrared Space Observatory (ISO) survey (van Dishoeck et al. 1998). Symbols refer to regional features discussed in this work. The position of "2" for IRc2 is at the EXES beam center for all settings in this survey. The location of BN is from Gomez et al. (2005). All other symbols, source I, source n, IRc3, IRc4, and IRc7, are placed according to Okumura et al. (2011). Refer to Figure 9 for a close-up of the IRc2 region.

small regions of warm, dense, molecular-rich gas associated with massive star formation. Their molecular richness arises from the evaporation of the molecular species off the icy dust grains in the cold molecular clouds (van Dishoeck & Blake 1998; Kurtz et al. 2000; van der Tak 2004; Cesaroni 2005; Beltrán & Rivilla 2018). Hot cores are most commonly internally heated by massive protostars (van der Tak 2004) though externally heated hot cores also exist (e.g., Mookerjea et al. 2007; Qin et al. 2022). Evidence suggests that the Orion hot core is externally heated (Blake et al. 1996; Orozco-Aguilera et al. 2017), possibly as a preexisting dense region of gas heated by either source I or the explosive event (Goddi et al. 2011; Zapata et al. 2011; Wright & Plambeck 2017). A few works argue that the hot core could be internally heated by an embedded protostar due to its high densities and temperatures (Kaufman et al. 1998; de Vicente et al. 2002; Wilkins et al. 2022).

Spectroscopic observations in the mid-infrared (MIR) are significantly fewer than longer-wavelength surveys of Orion BN/KL. However, rovibrational transitions and molecules with no permanent dipole moment are uniquely observable in the MIR. Observations toward an MIR-bright source reveal absorption lines originating in the gas between the source and the observer. This creates a pencil-beam effect in which the gas is probed in an area equivalent to the source, which can be much smaller than the telescope's beam size. The bright MIR source Orion IRc2 probes the edge of the hot core (Figure 1), either illuminating it from behind or coincident with it (Shuping et al. 2004). The hot core's NH$_3$ column density at IRc2 is about $30\% \pm 10\%$ of the value at the hot core's peak (Genzel et al. 1982; Wynn-Williams et al. 1984).

Orion IRc2 was first identified as a compact infrared source, the second brightest in the region after BN in the MIR (Rieke et al. 1973). Its nature remains unclear. Orion BN/KL may be a hollow nebula in which IRc2 is a cavity (Wynn-Williams et al.

1984). High spatial resolution imaging at 12.5 μm shows that IRc2 is U-shaped and breaks down into four pointlike sources (Shuping et al. 2004). The temperature distribution reveals a gradient that peaks close to source I, suggesting that IRc2 may be externally heated by it (Okumura et al. 2011). Polarimetry, however, suggests that source n may be illuminating IRc2 instead (Simpson et al. 2006).

Ground-based, high-resolution MIR spectroscopy toward Orion IRc2 contributed to the discovery of interstellar C$_2$H$_2$ and CH$_4$ (Lacy et al. 1989, 1991) with IRSHELL at the NASA Infrared Telescope Facility (IRTF; resolution $R \sim 10,000$; Lacy et al. 1989). Further IRTF/IRSHELL observations toward Orion IRc2 detected C$_2$H$_2$, ^{13}CCH$_2$, HCN, OCS, CO, and NH$_3$ (Evans et al. 1991; Carr et al. 1995). The Short-Wavelength Spectrometer (SWS) aboard the space-based Infrared Space Observatory (ISO; $R \sim 1500$; de Graauw et al. 1996) covered the entire MIR spectrum toward IRc2, from 2.4–45.2 μm. That work detected numerous features, including in absorption HCN and C$_2$H$_2$, as well as in emission H$_2$, CH$_4$, and SO$_2$. H$_2$O is observed in both emission and absorption (van Dishoeck et al. 1998; Wright et al. 2000; Boonman et al. 2003). These space-based spectral observations, while broad in coverage, were low resolution, and most absorption lines were blended into larger features. Inversely, the ground-based IRSHELL observations resolved individual transitions and had a better spatial resolution, but were limited by small coverage and interference from the Earth's atmosphere. These earlier studies had insufficient data to pinpoint the origins of the molecular MIR absorption lines toward IRc2.

In this work, we present the first high-resolution MIR line survey in the Orion BN/KL region toward IRc2, with nearly continuous coverage from from 7.2–8 μm and 12.8–28.3 μm taken with the EXES instrument ($R \sim 60,000$; Richter et al. 2018) on board the SOFIA observatory (Young et al. 2012). We supplement this SOFIA/EXES survey with a small amount of IRTF/TEXES ($R \sim 100,000$; Lacy et al. 2002) data from 11.7–11.9 μm.

Figure 1 shows EXES's much smaller beam size compared to that of ISO/SWS (van Dishoeck et al. 1998). While EXES is able to isolate Orion IRc2, several MIR-bright objects fall within SWS's beam. Figure 2 compares the resolution between EXES and SWS, illustrating that EXES has about 30 times higher spectral resolution than SWS and JWST/MIRI.

Our results build on previous 12.96–13.33 μm SOFIA/EXES observations toward IRc2 (Rangwala et al. 2018), and a segment of this survey was previously published covering HCN and the first MIR detections of HNC and H^{13}CN in the interstellar medium (Nickerson et al. 2021). This work complements EXES and TEXES observations toward the conventional protostar-harboring hot cores AFGL 2591, AFGL 2136 (4–13 μm; Indriolo et al. 2015; Barr et al. 2020, 2022; Indriolo et al. 2020), NGC 7538 IRS 1 (7.6–13.7 μm; Knez et al. 2009), and Mon R2 (7.23–7.38 μm; Dungee et al. 2018). Combined, these works and this present work provide a unique window into the chemistry and physical conditions in the massive star-forming regions that may shed light on our own solar system's origins (Adams 2010).

In Section 2 we describe this survey's observations, and Section 3 we detail analysis and provide results. In Section 4 we discuss the this survey's findings. Section 5 concludes this work.
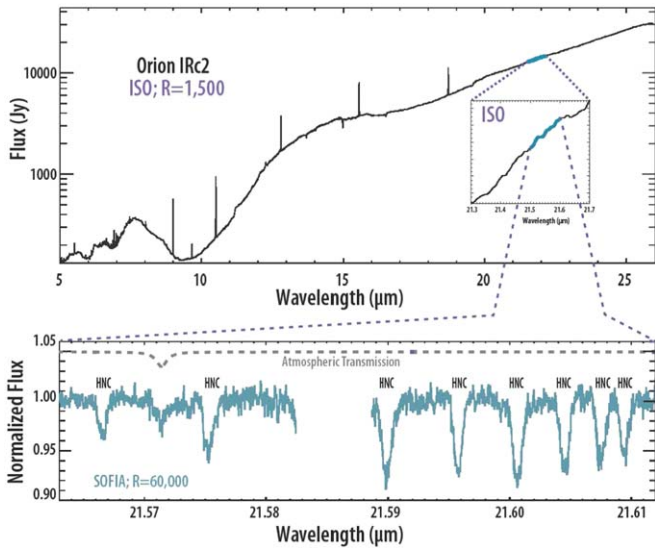
Figure 2. Comparison of resolution between MIR surveys toward Orion IRc2. Top: ISO/SWS, resolution ∼1500 (van Dishoeck et al. 1998), which will be similar to JWST/MIRI at this wavelength. Bottom: a segment of spectra with HNC absorption lines taken with SOFIA/EXES as part of this survey, resolution ∼60,000. With JWST/MIRI, these lines would be indiscernible from the continuum. Credit: NASA/SOFIA/M. Rose/N. Rangwala.

2. Observations

We observed Orion IRc2 with the EXES instrument aboard the SOFIA observatory between 2017 March 17 and 22, 2018 October 26 and November 11, and 2020 February 6 and 7, at altitudes normally above 39,000 ft. SOFIA flies above 99% of the Earth's atmospheric water vapor, covering wavelengths that are inaccessible from the ground.

All settings were taken in High-low mode, with the exception of the 7.3 μm setting in High-medium mode. Spectra were acquired in the cross-dispersed high-resolution mode with a slit width of 3″2, giving a resolving power of about 60,000 (∼5 km s^{-1}). We used the cross-disperser grating in first order to obtain the broadest simultaneous wavelength coverage per spectral setting. The slit length varied between 2″2 and 12″5, depending on the spectral setting. Table 1 gives the details for these settings, each of which is divided into several orders. For all observations, we nodded the telescope to an off-source position relatively free of emission 15″ east and 25″9 north of IRc2, at 1 minute intervals, in order to remove sky emission and thermal background from the telescope system. Two settings appear twice: 7.6a/b μm and 17.7a/b μm. The 7.6a μm setting was observed in 2018 October, and we noticed asymmetries in the atmospheric CH$_4$ lines. We revisited this setting in 2020 February (7.6b μm) with a Doppler shift favorable to capturing the CH$_4$ lines. Accordingly, we use only 7.6b for CH$_4$ analysis. The 17.7 μm setting was observed on two separate nights, but because no molecular lines were observed, we did not go further with analysis to combining the two nights.

The EXES data were reduced by the SOFIA Redux pipeline (Clarke et al. 2015). Wavelength scales were calibrated using sky emission line spectra produced for each setting by omitting the nod subtraction step and then adjusting the scale to match observed sky emission line wavelengths to their values in the HITRAN database (Gordon et al. 2017). The wavelength uncertainty is 0.3 km s^{-1}, estimated by comparing atmospheric emission lines to their wavelengths in the HITRAN database. Figures 10–13 in Appendix A show examples of normalized

flux with molecular lines for each species with atmospheric models.

The flux peak of IRc2 is known to shift in position at different MIR wavelengths (e.g., Gezari 1992; Greenhill et al. 2004; Okumura et al. 2011). To ensure the survey had a consistent center, all EXES observations began by acquiring flux peak as seen at 7.8 μm and maintaining that pointing during the observation legs. Figure 14 in Appendix B gives the EXES beam location, size, and orientation for each setting in this work. The edge of the EXES beam fell over nearby IR source, IRc7, for settings 20.5 μm through to 24.7 μm and 7.3 μm. After examining spectra split along the slit width, we confirm that the spectral lines are strong over the slit center at IRc2, and not the edge over IRc7. Furthermore, with ground-based MIR spectroscopy, Evans et al. (1991) found that C$_2$H$_2$ and HCN have two and three times higher column densities, respectively, toward IRc2 than IRc7. Therefore, these observations are centered over IRc2, and it is highly unlikely that any lines come from IRc7.

The SOFIA point-spread function size is about 3″–3″5 and rises to 4″ at the long wavelength limit for EXES. Thus for settings (Table 1) with slit sizes near this size or smaller, it is sensible to extract the spectrum over the entire available slit length, because any spatial information gets averaged together by the observatory seeing. This alone does not ensure that the exact same material is probed because the brightest part of the continuum of IRc2 moves depending on wavelength as explained above, especially for observations with longer slits. However, we inspected the spectra as extracted from three sectors along the slit and found little impact on the absorption lines, even for the longer slit lengths (the one exception is the sole H$_2$O absorption line, which will be discussed in Section 4.2.5). Because of this, we choose to sum over the entire slit for each setting in order to improve signal-to-noise for a better parameter estimation. Furthermore, as discussed in Section 4.1, the kinematic components probed by our observations may be spatially extended beyond IRc2 and in this case, the slightly differing location of our pencil beam is still probing the same kinematic component.

We supplement this EXES survey toward Orion IRc2 with two settings at 11.76 and 11.83 μm, taken with the TEXES (Lacy et al. 2002) instrument on the nights of 2018 February 8 and 11 at the NASA IRTF on Maunakea. This small amount of data fell within an atmospheric window in which SOFIA is comparable to ground-based observations and contains NH$_3$. We used high-medium mode with a resolution of about 100,000 (∼3 km s^{-1}) and a beam sized 8″ × 1″4 oriented north–south. The beam was centered on the continuum peak of IRc2 for the wavelength of each setting. The telescope nodded 3″ along the slit to enable background subtraction. The flux was extracted by weighting the signal by the continuum flux distribution.

3. Analysis and Results

3.1. Flux Preparation

We normalize the EXES data following the procedure detailed in Nickerson et al. (2021). Here we summarize it briefly. In the raw EXES flux and an unsmoothed ATRAN atmospheric transmission model (Lord 1992),[12] we identify

---

[12] https://atran.arc.nasa.gov/cgi-bin/atran/atran.cgi

Table 1
Specifications for Each Setting

Setting (μm)	Species	Min λ (μm)	Max λ (μm)	Date (yyyy-mm-dd)	Configuration	Slit Length (″)	Integration Time (s)
				SOFIA/EXES (slit width: 3″2)			
7.3	C_2H_2, H_2O[a], HCN, SO_2	7.2	7.3	2020-02-06	High-med	8.3	5888
7.6a	C_2H_2, H_2O[a]	7.5	7.7	2018-10-26	High-low	3.4	8196
7.6b	C_2H_2, CH_4, H_2O[a]	7.5	7.7	2020-02-07	High-low	3.4	7296
7.8	CS, H_2O[a]	7.7	7.9	2018-10-31	High-low	3.6	8064
7.9	CS, H_2O[a], SiO[a]	7.8	8.0	2018-11-01	High-low	3.8	4608
13.2	C_2H_2, $^{13}CCH_2$, HCN, [Ne II][a, c]	12.8	13.6	2018-10-31	High-low	2.2	2560
13.9	C_2H_2, $^{13}CCH_2$, HCN, $H^{13}CN$	13.5	14.3	2018-10-30	High-low	2.4	2880
16.3	⋯	15.9	16.7	2018-10-30	High-low	3.3	2816
17.0	H_2[a]	16.6	17.4	2018-10-30	High-low	3.7	1024
17.7a	⋯	17.2	18.0	2018-10-27	High-low	4.3	512
17.7b	⋯	17.2	18.0	2018-10-30	High-low	4.5	768
18.4	SO_2	17.9	18.7	2018-10-27	High-low	4.7	768
19.1	SO_2, [S III][a, c]	18.7	19.4	2018-10-27	High-low	5.3	1024
19.8	SO_2	19.4	20.1	2018-10-27	High-low	5.4	704
20.5	HNC, SO_2	20.1	20.8	2018-10-27	High-low	6.0	576
21.2	HNC	20.8	21.5	2018-10-27	High-low	6.4	512
21.9	HNC	21.5	22.2	2018-10-27	High-low	7.0	512
22.6	HNC	22.2	22.9	2018-10-27	High-low	7.7	512
23.3	⋯	22.9	23.6	2018-10-27	High-low	8.3	384
23.9	⋯	23.5	24.2	2018-10-26	High-low	8.7	352
24.7	OH[b]	24.3	24.9	2018-10-26	High-low	9.4	448
25.3	[S I][c, b]	24.9	25.7	2017-03-22	High-low	9.6	1920
26.0	H_2O, [Fe II][a, d]	25.6	26.3	2017-03-22	High-low	10.2	1856
26.7	⋯	26.2	26.9	2017-03-17	High-low	10.4	1280
27.4	⋯	26.9	27.6	2017-03-17	High-low	11.5	1280
28.1	⋯	27.6	28.3	2017-03-17	High-low	12.5	1728
				IRTF/TEXES (slit width: 1″4)			
11.76	NH_3	11.71	11.81	2018-02-08	High-med	8	2331
11.83	NH_3	11.78	11.89	2018-02-11	High-med	8	2331

Notes.
[a] denotes emission line. All other lines are in absorption.
[b] denotes a tentative detection.
[c] denotes lines observed in both the on- and off-source positions.
[d] denotes a line observed only in the off-source position. All other lines are observed only in the on-source position towards IRc2. ⋯ denotes no detected lines in that setting.

baselines, noise, atmospheric lines, and molecular lines toward IRc2 both with algorithms and by hand where algorithms are insufficient. We fit the baseline and atmospheric line segments in the raw flux and the atmospheric model to find the constant by which to normalize the flux in each order and the sigma in each setting by which to Gaussian smooth the atmospheric model's lines. This normalized flux will match the smoothed atmospheric model as closely as possible, aside from noise in the flux and the atmospheric model's limitations. Some molecular lines fall near to atmospheric lines, and we divide the flux by the atmospheric model to recover molecular lines. The exceptions are the HNC and SO_2 lines, which do not require the division.

Additionally, a number of orders in settings 13.2, 20.5, 21.9, and 22.6 μm exhibit uneven baselines from standing waves and require division by a polynomial in order to flatten the baseline. The upper-right panel in Figure 10 is an example of an uncorrected standing wave in the baseline, while the bottom-left panel in Figure 10 is an example of a baseline post-polynomial correction.

The small quantity of TEXES data included in this paper has already been normalized by the instrument team from division by an atmospheric model. We do not need to correct it further.

3.2. Single Lines

For all species, except SO_2 (Section 3.3), we fit individual lines to Gaussians to extract their column densities for rotation diagram analysis.

The majority of this survey's species are absorption lines, analyzed following the procedure detailed in Nickerson et al. (2021). Briefly summarized here, we fit with a Gaussian profile following Indriolo et al. (2015):

$$I = I_0 e^{-\tau_0 G}, \quad (1)$$

where,

$$G = \exp\left[-\frac{(v - v_{\mathrm{LSR}})^2}{2\sigma_v^2}\right], \quad (2)$$

I_0 is the normalized continuum level (close to unity), τ_0 is the line center optical depth, v is the velocity in the local standard of rest (LSR) frame, v_{LSR} is the LSR velocity at the line's center, and σ_v is the velocity dispersion (FWHM $v_{\mathrm{FWHM}} = 2\sqrt{2\ln 2}\,\sigma_v$).

One Gaussian is the optimal fit for CS, H_2O, HNC, $H^{13}CN$, and NH_3, resulting in only one apparent velocity component.
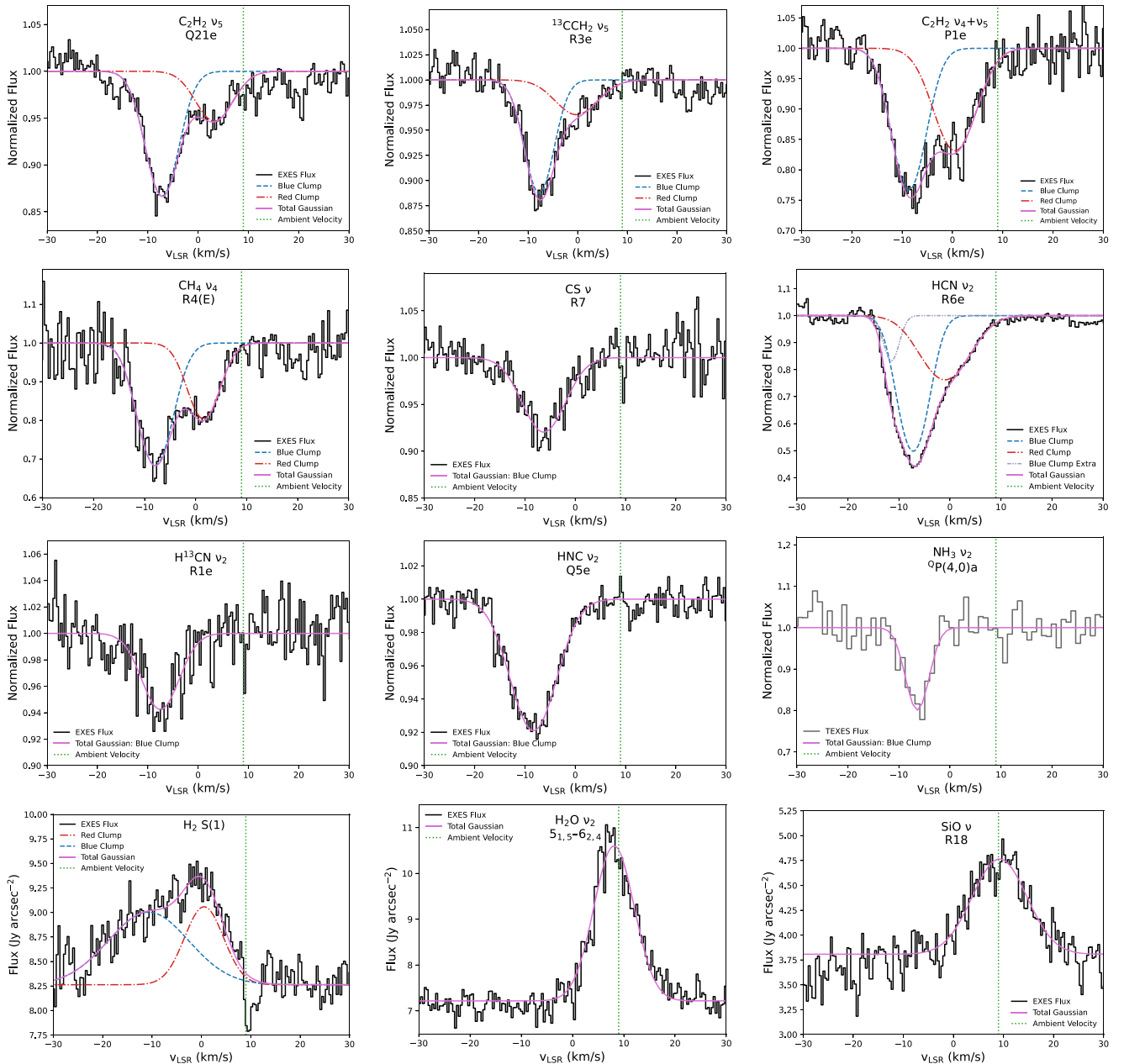
Figure 3. Sample Gaussian fits, left to right and top to bottom, for the ν_5 band of C_2H_2, $^{13}CCH_2$, the $\nu_5 + \nu_4$ band of C_2H_2, CH$_4$, CS, HCN, H^{13}CN, HNC, NH$_3$, H$_2$, H$_2$O, and SiO. Black is EXES flux and gray is TEXES flux. Fluxes are normalized for absorption lines and in janskys per arcsecond^2 for emission lines. Magenta is the total Gaussian fit, while for double and triple Gaussians, the blue, red, and lavender dashed–dotted lines belong, respectively, to the blue clump, the red clump, and in this example, extra for the blue clump. Single-component fits belong to the blue clump for the absorption lines. The vertical, green dotted line indicates the systematic, ambient cloud velocity 9 km s^{-1} (Zapata et al. 2012).

The species C_2H_2, $^{13}CCH_2$, CH$_4$, and HCN, have two apparent velocity components and were best fit by double Gaussians:

$$I = I_0 e^{-(\tau_{01}G_1 + \tau_{02}G_2)}. \quad (3)$$

It is not possible, however, to fit every single line from these species to double Gaussians. Some have only single Gaussians, particularly if the line is weak, suffers from atmospheric interference, or blends with another molecular line.

We give the examples of these fits for each species in Figure 3. The absorption species fit two distinct kinematic components, with average $v_{LSR} = -7.1 \pm 0.7$ km s^{-1} and 1.4 ± 0.5 km s^{-1}, which we refer to for convenience as the "blue clump" and the "red clump" due to their blue- and

redshifted velocities relative to the LSR. Both are blueshifted with respect to the ambient cloud velocity, 9 km s^{-1} (Zapata et al. 2012). The single Gaussian species (CS, H$_2$O, HNC, H^{13}CN, and NH$_3$) all belong to the blue clump, while the species with transitions best fit to double Gaussians (C_2H_2, $^{13}CCH_2$, CH$_4$, and HCN) have a deeper Gaussian that belongs to the blue clump and a shallower Gaussian that belongs to the red clump. This is the first work that unambiguously identifies the blue and red clumps in detail. We discuss these two components further in Section 4.1 and compare their properties in Table 5.

Some lines for HCN, C_2H_2, and $^{13}CCH_2$ that coincide with the telluric features are distorted even after the atmospheric

Table 2
Overview of Species Properties

Species	Band (μm)	Component	#	v_{LSR} (km s^{-1})	v_{FWHM} (km s^{-1})	T (K)	N cm^{-2}
C$_2$H$_2$ Ortho	ν_5 13.5	Blue Clump	24	-7.3 ± 0.1	8.5 ± 0.1	175 ± 12	$(1.50 \pm 0.15)\times10^{16}$
		Red Clump	17	1.4 ± 0.2	7.5 ± 0.2	229 ± 27	$(3.58 \pm 0.71)\times10^{15}$
Para	ν_5 13.5	Blue Clump	20	-7.5 ± 0.0	8.1 ± 0.1	145 ± 9	$(1.23 \pm 0.15)\times10^{16}$
		Red Clump	12	1.8 ± 0.2	7.0 ± 0.3	158 ± 16	$(3.09 \pm 0.57)\times10^{15}$
^{13}CCH$_2$	ν_5 13.5	Blue Clump	10	-7.4 ± 0.1	7.2 ± 0.4	91 ± 9	$(2.56 \pm 0.18)\times10^{15}$
		Red Clump	4	2.1 ± 1.0	8.2 ± 1.7	64 ± 6	$(6.74 \pm 0.64)\times10^{14}$
C$_2$H$_2$ Ortho	$\nu_4 + \nu_5$ 7.6	Blue Clump	8	-7.5 ± 0.1	8.2 ± 0.2	124 ± 13	$(8.39 \pm 1.44)\times10^{16}$
		Red Clump	8	1.3 ± 0.2	7.5 ± 0.3	111 ± 14	$(4.73 \pm 1.06)\times10^{16}$
Para	$\nu_4 + \nu_5$ 7.6	Blue Clump	5	-7.9 ± 0.2	8.2 ± 0.4	73 ± 14	$(3.42 \pm 0.73)\times10^{16}$
		Red Clump	5	1.3 ± 0.3	7.3 ± 0.6	140 ± 18	$(2.50 \pm 0.21)\times10^{16}$
CH$_4$	ν_4 7.6	Blue Clump	6	-8.0 ± 0.1	7.6 ± 0.3	193 ± 42	$(1.99 \pm 0.28)\times10^{17}$
		Red Clump	6	0.6 ± 0.2	7.9 ± 0.4	141 ± 33	$(8.80 \pm 1.78)\times10^{16}$
CS	ν 7.8	Blue Clump	9	-6.4 ± 0.1	8.6 ± 0.5	175 ± 34	$(6.97 \pm 0.58)\times10^{15}$
H$_2$*	17	Blue Clump	1	-10.7 ± 2.6	19.2 ± 5.1	$\cdots$	$\cdots$
		Red Clump	1	0.5 ± 0.5	9.3 ± 1.8	$\cdots$	$\cdots$
H$_2$O	26	Blue Clump	1	-8.0 ± 0.4	17.0 ± 1.0	$\cdots$	$\cdots$
H$_2$O*a	ν_2 7.6	$\cdots$	13	8.8 ± 0.1	10.6 ± 0.2	$\cdots$	$\cdots$
HCN	ν_2 13.5	Blue Clump	22	-7.3 ± 0.0	8.7 ± 0.1	135 ± 9	$(5.44 \pm 0.43)\times10^{16}$
		Red Clump	15	1.0 ± 0.2	8.3 ± 0.4	182 ± 34	$(1.87 \pm 0.39)\times10^{16}$
	$2\nu_2$ 7.0	Blue Clump	2	-5.8 ± 0.6	8.7 ± 1.0	$\cdots$	$\cdots$
		Red Clump	2	1.8 ± 0.9	6.4 ± 1.4	$\cdots$	$\cdots$
H^{13}CN	ν_2 13.5	Blue Clump	3	-6.6 ± 0.2	7.9 ± 0.5	99 ± 16	$(4.36 \pm 0.65)\times10^{15}$
HNC	ν_2 22	Blue Clump[b]	24	-7.7 ± 0.1	11.3 ± 0.2	97 ± 8	$(7.41 \pm 0.62)\times10^{14}$
NH$_3$	ν_2 11	Blue Clump	5	-6.7 ± 0.4	6.7 ± 1.3	230 ± 86	$(1.58 \pm 0.77)\times10^{16}$
SiO*a	ν 7.9	$\cdots$	12	9.8 ± 0.1	13.6 ± 0.4	$\cdots$	$\cdots$
SO$_2$	ν_2 19	Blue Clump[b]	$\cdots$	$-6.1^{+0.5}_{-0.5}$	$12.9^{0.9}_{0.9}$	94^{+7}_{-6}	$(6.17^{+0.44}_{-0.42}) \times 10^{16}$
	ν_3 7.2	Blue Clump[b]	$\cdots$	$-6.0^{+0.3}_{-0.3}$	$11.2^{+0.5}_{-0.5}$	128^{+5}_{-5}	$(1.10^{+0.03}_{-0.03}) \times 10^{17}$

Notes. For each species, band, and velocity component: # is the number of lines, v_{LSR} is the average central local standard rest of velocity, v_{FWHM} is the average FWHM, T is the temperature, and N is the total column density. Note that the H$_2$O and H$_2$ transitions with no band are pure rotational. * denotes emission line.
[a] The temperatures and column densities of the H$_2$O and SiO emission will appear in a future publication.
[b] HNC and SO$_2$ have wide enough line widths that there may be an unresolved red clump component in the data, as discussed in Section 4.1.

division. Many of these require fits to a triple Gaussian, which follows similarly from Equation (3). The third Gaussian components are either discarded or absorbed into the red or blue clump component, depending on the line shape. For these lines we take the line with the deepest τ_0 to provide the LSR velocity for the combined line. We also do not include these lines for calculating the mean v_{FWHM} for the species in Table 2, because the Gaussians overlap. See the HCN Gaussian fit in Figure 3 for an example of this situation.

For absorption lines, we calculate the column density, N_l, in the lower state of an observed transition as follows for the optically thin limit:

$$N_l = \sqrt{2\pi}\, \frac{g_l}{g_u} \frac{8\pi}{A\lambda^3} \tau_0 \sigma_v, \qquad (4)$$

where g_l and g_u are the lower and upper statistical weights, respectively, A is the Einstein coefficient for spontaneous emission, and λ is the rest wavelength of the transition.

Emission lines are analyzed following a procedure that will be detailed and derived in a future publication. There, we will also present the full analysis of the H$_2$O and SiO emission lines. In this work, we present the results for the two-component H$_2$ line. We obtained the H$_2$ spectrum in units of ergs/(s cm^2 sr cm^{-1}) by averaging along the row in the coadded image, and multiplying by a conversion factor, S_{Ja}, to obtain the spectrum in units of janskys per arcsecond^2. We fit the H$_2$ line to the following double Gaussian:

$$S_\nu(v) = B_\nu + S_{\nu01} \exp\left(\frac{-(v - v_{LSR1})^2}{2\sigma_{v1}^2} \right) \qquad (5)$$

$$+ S_{\nu02} \exp\left(\frac{-(v - v_{LSR2})^2}{2\sigma_{v2}^2} \right), \qquad (6)$$

where B_ν is the continuum level, and corresponding to Gaussians 1 and 2: $S_{\nu01}$ and $S_{\nu02}$ are the amplitudes, v_{LSR1} and v_{LSR2} are the LSR velocities of the line centers, and σ_{v1} and σ_{v2}

are the velocity dispersions. We calculate N_u, the upper state column density, for each Gaussian, as follows:

$$N_u = \frac{4\pi\sqrt{2\pi}\, S_{Ja} S_{\nu 0} \sigma_\nu}{hcA}. \tag{7}$$

The observed transitions and inferred parameters for all transition lines are given in Appendix D: molecular absorption lines in Table 11 and molecular emission lines in Table 12. Errors are generated by the fitting routine. We note dividing out the atmosphere from some lines does introduce uncertainly as well, but because we cannot quantify the accuracy of the ATRAN model, we also cannot quantify the error introduced by this process.

The level populations of molecules in local thermal equilibrium (LTE) follow the Boltzmann distribution (Goldsmith & Langer 1999):

$$\ln\frac{N_l}{g_l} = \ln\frac{N}{Q_R(T)} - \frac{E_l}{k_B T}, \tag{8}$$

where N_l is the column density of the lower state, g_l is the statistical weight of the lower state, N is the total column density, Q_R is the rotational partition function, E_l is the energy level of the lower state, T is the temperature, and k_B is the Boltzmann constant. Because we assume LTE, the temperature is equivalent to the kinetic temperature of the gas. The above applies to absorption lines where we use the lower state values, and for the H_2 emission line, we use the upper state values instead, denoted by a subscript "u". λ, A, g_l, g_u, Q_R, E_l, and E_u for each molecular transition come from three databases. We use GEISA (Jacquinet-Husson et al. 2016) and our own calculations for Q_R for HNC from levels published in ExoMol (Harris et al. 2006; Barber et al. 2013), ExoMol (Tennyson & Yurchenko 2012) for SiO, and HITRAN (Gordon et al. 2017) for all other species.

By linearly fitting to Equation (8), we obtain the values of T and N for each species and velocity component, summarized in Table 2. Full rotation diagram analysis with the column densities and temperatures for the H_2O and SiO emission lines will appear in a future publication.

To calculate abundances (Table 3), we use the column density range estimated by Evans et al. (1991) along the line of sight toward Orion IRc2, $N_{H_2} = (1.9 \pm 1.1) \times 10^{23}$ cm^{-2}. This upper limit was based on NH_3 mapping of the region, in which IRc2 was calculated to probe about 30% of the material in the densest part of the hot core (Wynn-Williams et al. 1984), while the lower limit was found by calculating the depth of the silicate feature. Because this column density measures the total H_2 toward IRc2 and not individual components, we sum the column density of both the blue and red clumps when calculating abundances. The H_2 emission lines may also trace the same gas as the red and blue clumps, having similar velocities. However, we do not use them to calculate abundance ratios due to the uncertainty associated with a single transition. We discuss H_2 further in Section 4.2.4.

Figures 4–6 give the rotation diagrams for absorption species. We fit all three branches, P, Q, and R, to a single line. For C_2H_2, we treat the ortho and para ladders as separate species fit by separate lines, as in Rangwala et al. (2018). The species generally show a linear relationship between $\ln(N_l/g_l)$ and E_l/k_B, implying that the LTE approximation holds.

The one exception is that the Q branch of the C_2H_2 ν_5 band in the blue clump flattens toward lower transition energies. A number of these lines are compromised by proximity to

Table 3
Abundance Ratios

Species	Band	N/N_{H_2}
C_2H_2 Ortho	ν_5	$(9.78 \pm 5.73) \times 10^{-8}$
C_2H_2 Para	ν_5	$(8.10 \pm 4.76) \times 10^{-8}$
$^{13}CCH_2$	ν_5	$(1.70 \pm 0.99) \times 10^{-8}$
C_2H_2 Ortho	$\nu_4 + \nu_5$	$(6.91 \pm 4.11) \times 10^{-7}$
C_2H_2 Para	$\nu_4 + \nu_5$	$(3.12 \pm 1.85) \times 10^{-7}$
CH_4	ν_4	$(1.51 \pm 0.89) \times 10^{-6}$
CS	ν	$(3.67 \pm 2.15) \times 10^{-8}$
HCN	ν_2	$(3.85 \pm 2.25) \times 10^{-7}$
$H^{13}CN$	ν_2	$(2.29 \pm 1.37) \times 10^{-8}$
HNC	ν_2	$(3.90 \pm 2.28) \times 10^{-9}$
NH_3	ν_2	$(8.32 \pm 6.29) \times 10^{-8}$
SO_2	ν_2	$(3.25 \pm 1.89) \times 10^{-7}$
SO_2	ν_3	$(5.79 \pm 3.36) \times 10^{-7}$

Note. The column density, N, for each species is the sum of both the blue and red clumps, and N_{H_2} is the column density of H_2 along the line of sight toward IRc2, $1.9 \pm 1.1 \times 10^{23}$ cm^{-2} (Evans et al. 1991).

atmospheric lines (see Table 11), but another explanation might be that the Q branch of C_2H_2 exhibits non-LTE behavior. As explained in Rangwala et al. (2018), we rule out the need for a covering factor and optical depth effects, because our lines do not have flat bottoms and the optical depth varies without a cap. In high-resolution MIR spectra of H_2O toward the hot core AFGL 2136, Indriolo et al. (2020) noted that deeper transitions tend to be "underpopulated," possibly because the absorbing gas is mixed with emitting dust. We tested for this effect in our data, but found no correlation between optical depth and underpopulation.

Some rotation diagrams show much higher scatter than others (such as HCN being more scattered than HNC). This may be caused by imperfect atmospheric removal or other incompletely corrected artifacts in the data. Division with the ATRAN model cannot fully quantify how much the model deviates from observations. We do note however, that our fits to individual lines have evenly distributed residuals regardless of how impacted they were by the atmosphere. This means that the atmospheric correction had a systematic effect, either raising or lowering the flux of each affected line, thereby causing scatter in the rotation diagrams.

For HCN, HNC, and the ν_5 band of C_2H_2, the Q-branch transitions appear to be slightly weaker than the R-branch transitions. This may be due to an effect demonstrated by radiative transfer modeling in Lacy (2013): Q-branch absorption lines are weaker compared to the R branch by a factor of about $2/3$. There are not enough measured P-branch transitions to comment on those in our data, but Lacy (2013) expected their strength to be comparable to R-branch transitions.

3.3. Crowded Lines

SO_2 transitions are characteristically a dense forest that is too crowded to allow for rotation diagram analysis via fitting individual lines to Gaussians (Figure 12, bottom two panels). Instead, we fit simulated spectra to the normalized EXES flux using a Bayesian approach with the Markov Chain Monte Carlo (MCMC) ensemble sampler emcee (Foreman-Mackey et al. 2013).[13]

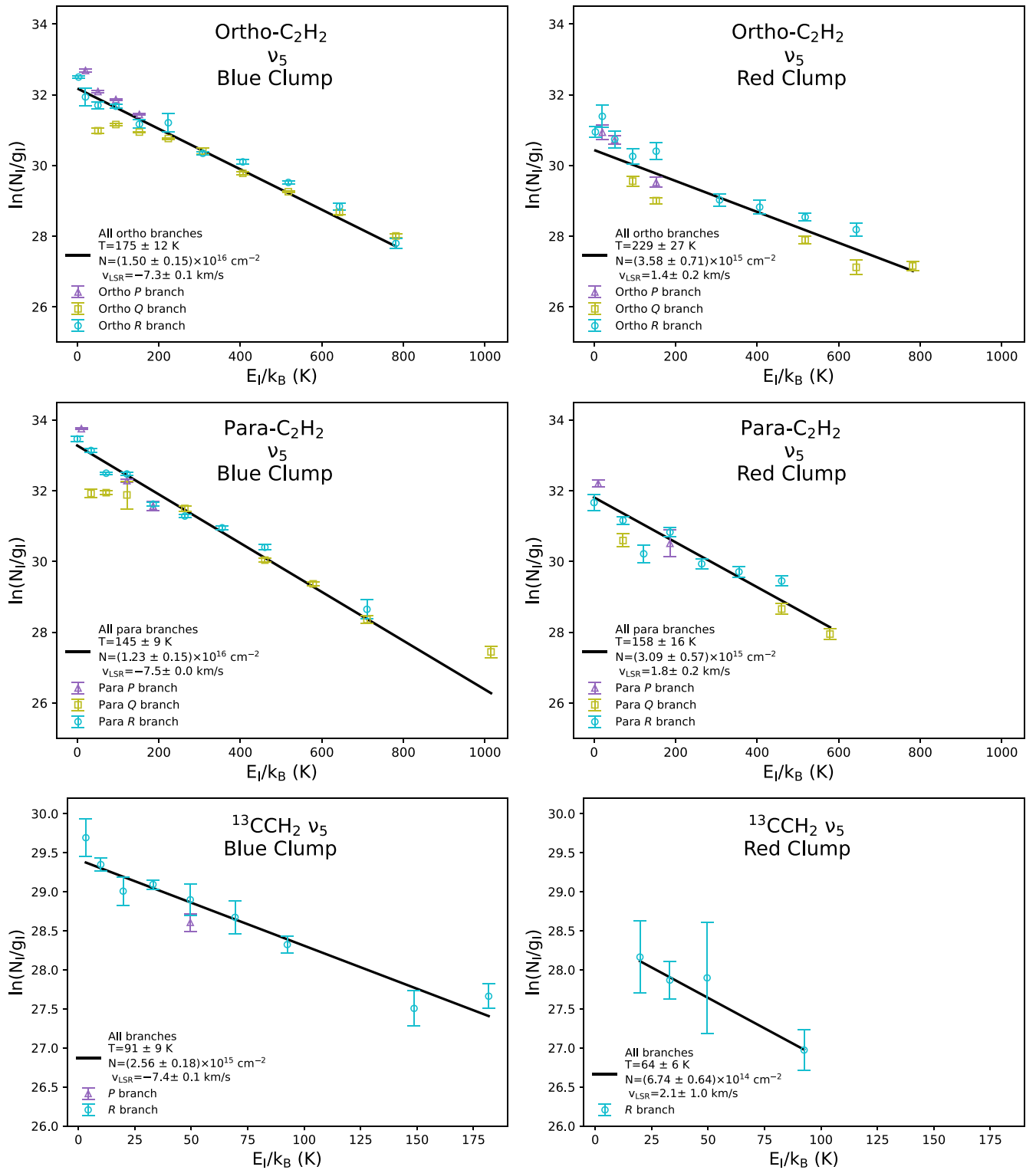---

[13] https://github.com/dfm/emcee

Figure 4. Rotation diagrams for the blue clump (left column) and red clump (right column): the ν_5 band of ortho-C_2H_2 (top row), the ν_5 band of para-C_2H_2 (middle row), and the ν_5 band of $^{13}CCH_2$ (bottom row).

We create the simulated spectra by working backwards from Equations (8), (4), and (1). Treating the total column density N, temperature T, line center LSR velocity v_{LSR}, and line width σ_ν as input variables along with the properties of each transition from HITRAN (Gordon et al. 2017), we generate simulated spectra that are a superposition of the Gaussian profiles of all transitions in the range of interest.

To prepare the normalized flux for fitting, we exclude from the flux regions of noise, atmospheric lines, or lines of other molecules. What remains is a "scrubbed" flux consisting of
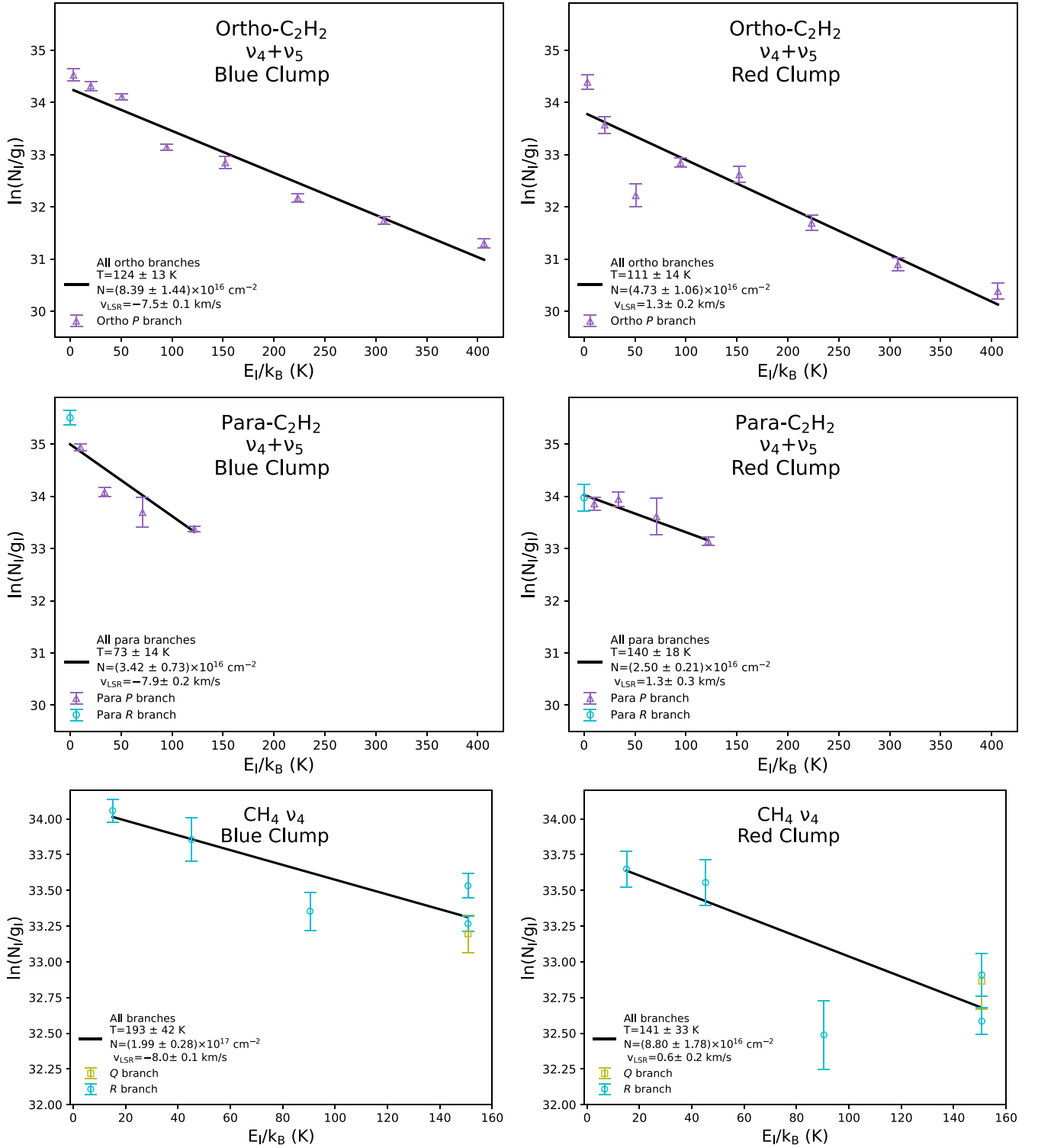
Figure 5. Rotation diagrams for the blue clump (left column) and red clump (right column): the $\nu_4 + \nu_5$ band of ortho-C_2H_2 (top row), the $\nu_4 + \nu_5$ band of para-C_2H_2 (middle row), and CH_4 (bottom row).

only the baseline and SO_2 transitions. We minimize the following likelihood function:

$$\sum_{i}^{\text{pixels}} \| F_{\text{sim},i}(\log(N), T, \sigma_\nu, v_{\text{LSR}}) - F_{\text{scrub},i} \|, \qquad (9)$$

where $F_{\text{sim},i}$ is the simulated flux at pixel i, and $F_{\text{scrub},i}$ is the scrubbed flux at pixel i. For minimization, we use the `scipy` routine `optimize.minimize` (Virtanen et al. 2020) to find the values for N, T, v_{LSR}, and σ_ν that generate a simulated spectra that most closely matches the scrubbed flux. These
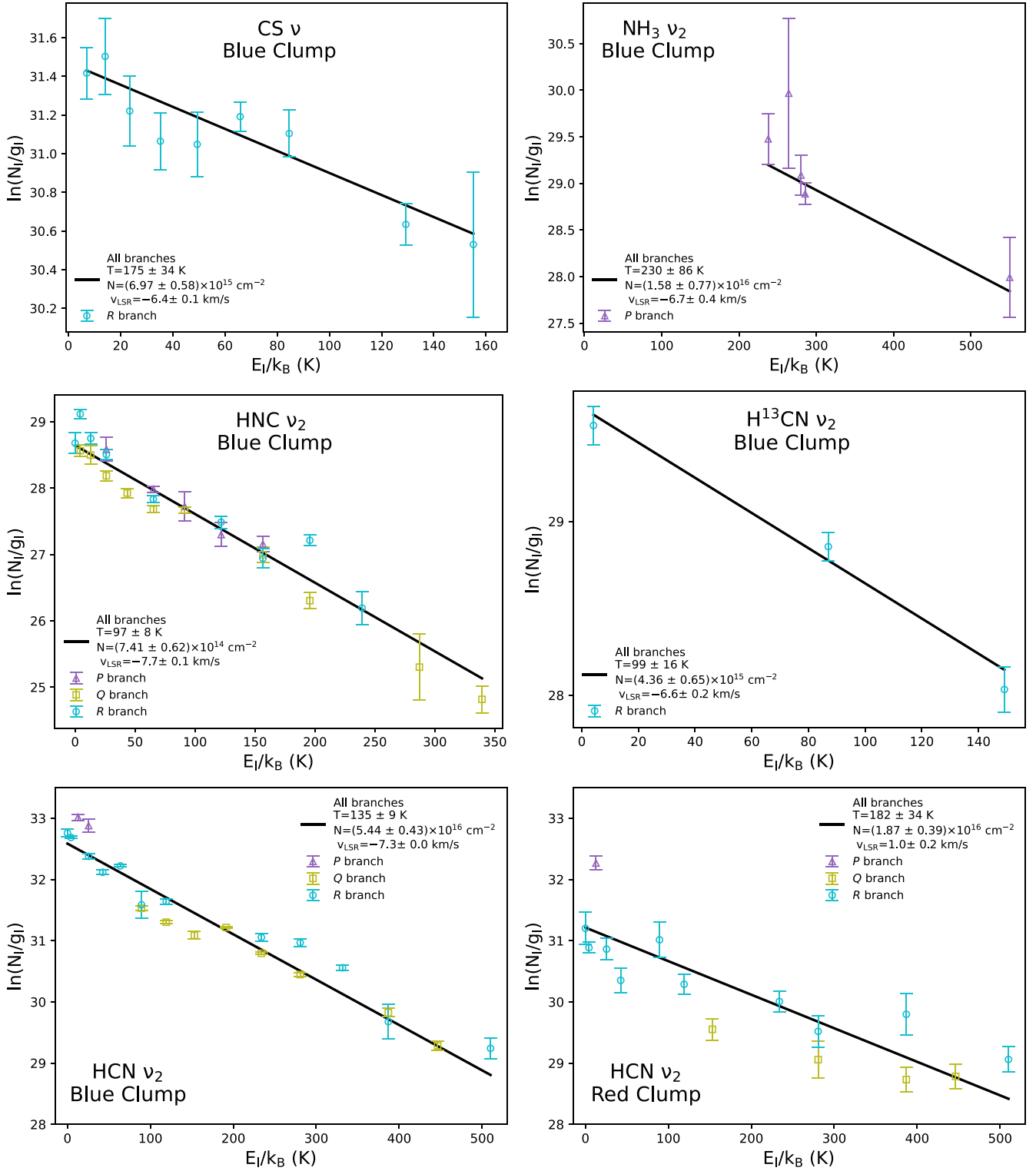
Figure 6. Rotation diagrams for: CS (top left), NH_3 (top right), HNC (middle left), $H^{13}CN$ (middle right), blue clump HCN (bottom left), and red clump HCN (bottom right).

results of the minimization provide sensible initial values for the MCMC sampler.

To set up the MCMC sampler, we adopt priors uniform over their limits for N, T, and v_{LSR}, and a normal distribution for σ_ν centered on the initial value, summarized in Table 4. Because $\tau_0 \propto N\sigma_\nu$, N, and σ_ν are not linearly independent, they will not work as separate variables with the MCMC sampler unless we

assume a nonuniform distribution for σ_ν. We use Equation (9) as the likelihood function, and the initial values are randomized in a normal distribution close to the results of the minimization.

The SO_2 transitions in the data occur at two distinct wavelengths regimes, settings 20.5–18.4 μm dominated by the ν_2 band, and setting 7.3 μm dominated by the ν_3 band. We run the MCMC sampler on these bands separately, with 64 walkers

Table 4
Prior Distribution Functions for the MCMC Sampler

Variable	Distribution	Min Value	Max Value
$\log(N)$	Uniform	1 cm^{-2}	50 cm^{-2}
T	Uniform	1 K	10^3 K
v_{LSR}	Uniform	-500 km s^{-1}	500 km s^{-1}
σ_ν	$(\sigma_\nu - \sigma_{\nu 0})^2$	0.001 km s^{-1}	50 km s^{-1}

Note. $\sigma_{\nu 0}$ is the initial value for σ_ν as determined by minimization.

and chains of 3000 steps each. Both bands converged after about 1000 steps. We excluded the 18.4 μm setting from the scrubbed flux for the ν_2 band due to it being noisier compared to the other settings. We nonetheless visually inspected the final result against this setting and found that the simulated spectra fit it well.

Figures 7 and 8 give the resulting posterior distribution of $\log(N)$, T, v_{LSR}, and σ_ν from the MCMC sampler for the ν_2 and ν_3 bands, respectively. For each variable, we take the 16th and 84th percentiles of the posterior distribution as the uncertainties around the median, as reported in Table 2. The bottom two panels of Figure 12 in Appendix A show the simulated spectra for each band. We tested both bands to see if a double Gaussian fit the data better, but it did not. Each band has a single absorption component that fits with the blue clump seen in other absorption lines.

3.4. Atomic Forbidden Transitions

The survey includes four features from atomic forbidden transitions: [Ne II] (12.81 μm), [S III] (18.71 μm), [S I] (25.25 μm), and [Fe II] (25.99 μm). These lines are all in emission, and, except for [Fe II], are in emission at both the off-source position and the on-source position toward IRc2 (see Section 2 for descriptions of the on- and off-source positions). [Fe II] is not found in emission or absorption toward IRc2, but is in emission at the off-source position leading to apparent absorption at the on-source position. These lines are shown in Figure 13 in Appendix A.

The [Ne II] and [S III] features are very strong even compared to the background emission, and the lines are fit with Gaussians using the separate on- and off-source data before subtraction. The [S III] profile toward the off-source position is not well fit by a single Gaussian and has an extended blue wing.

The [Fe II] profile shows emission in the off-source data, but because the emission is so weak compared to the background emission, the best fit is obtained by using the difference spectrum and inverting the apparent absorption spectrum to the actual emission spectrum.

The [S I] line is also weak compared to the background, and the instrumental bandpass is impossible to accurately remove in the individual on- and off-source spectra. The on-off difference spectrum removes the instrumental bandpass quite well and displays an "apparent" reverse P-Cygni profile, with the absorption and emission peaks well separated. Parameters for the [S I] Gaussian fits are obtained by individually fitting the "absorption" and emission features in the on-off difference spectrum, converting the absorption values to the equivalent emission values, and confirming that these fits are consistent with the more erratic profiles extracted from the individual on- and off-source spectra.

Table 13 in Appendix D gives the observed transitions and inferred parameters for the atomic and ion transition lines.

4. Discussion

4.1. Kinematic Components

Our work covers two new and distinct velocity components in the region, observed by absorption lines in the MIR: the blue clump with $v_{LSR} = -7.1 \pm 0.7$ km s^{-1} and the red clump with 1.4 ± 0.5 km s^{-1} (Figure 9). The top half of Table 5 shows for these two components the average v_{LSR}, v_{FWHM}, and temperatures as well as the species found in this work. While the blue and red clumps have a similar temperature (≈ 140 K) and v_{FWHM} (≈ 8 km s^{-1}), the v_{LSR} of each is distinct. The other striking difference between them is that species column densities in the blue clump are 1.37–4.19 times higher than in the red clump (Table 6). The column density ratio variance shows that the molecular ratios themselves vary in each clump, suggesting different locations and chemical evolution for the blue and red clumps. We discuss the H_2 emission line and its link to the blue and red clumps in Section 4.2.4. The bottom half of Table 5 summarizes the properties of the classic components in the region as observed from emission lines in longer-wavelength surveys: the hot core, the extended ridge, the compact ridge, and the plateau, as discussed in Section 1.

Because this survey is only pointed toward IRc2, it does not give any information on the spatial extent of the red and blue clumps. However, spectroscopic studies toward other targets offer clues.

Figure 7 in Lacy et al. (2002) illustrates the HCN R(11) and C_2H_2 R(7) absorption lines toward IRc2, IRc4, and IRc7 without analysis. The absorption lines toward IRc2 are clearly a double Gaussian with the blue and red clumps. The lines for IRc4 and IRc7 appear asymmetric, but because they are noisier, it is unclear if they show the red clump component. What is clear, however, is that the central velocities of the lines toward IRc4 and IRc7 closely match those of the blue clump toward IRc2. This suggests that the blue clump is at least extended enough to cover IRc4 and IRc7. Figure 9 shows a map of the morphology of IRc2, IRc4, IRc7, and source n as a segment of Figure 1.

There is evidence that the blue clump extends toward source n (Beuther et al. 2010). High-resolution spectroscopic observations toward source n with the Very Large Telescope (VLT)/ CRIRES from 4.59–4.72 μm revealed ^{13}CO absorption lines with $v_{LSR} = -7$ km s^{-1} and by rotation diagram analysis a temperature of 163 ± 20 K and column density 4.3×10^{18} cm^{-2}. The v_{LSR} matches the average for the blue clump almost exactly (-7.1 ± 0.7 km s^{-1}), while the temperature falls within the range of temperatures we measured with other species in the blue clump and the column density of ^{13}CO is higher compared to our species, which is expected. The ^{12}CO lines were saturated toward source n and were not analyzed in Beuther et al. (2010). We should also note that from the ^{13}CO measurements they estimated the total H_2 toward source n to be 1.4×10^{23} cm^{-2}, which falls within the range estimated by Evans et al. (1991) toward IRc2 ($N_{H_2} = (1.9 \pm 1.1) \times 10^{23}$ cm^{-2}), showing little variation in the H_2 column density toward these two objects. The same work covers IRc3, and there is no evidence for absorption lines matching the blue and red clumps toward this object.
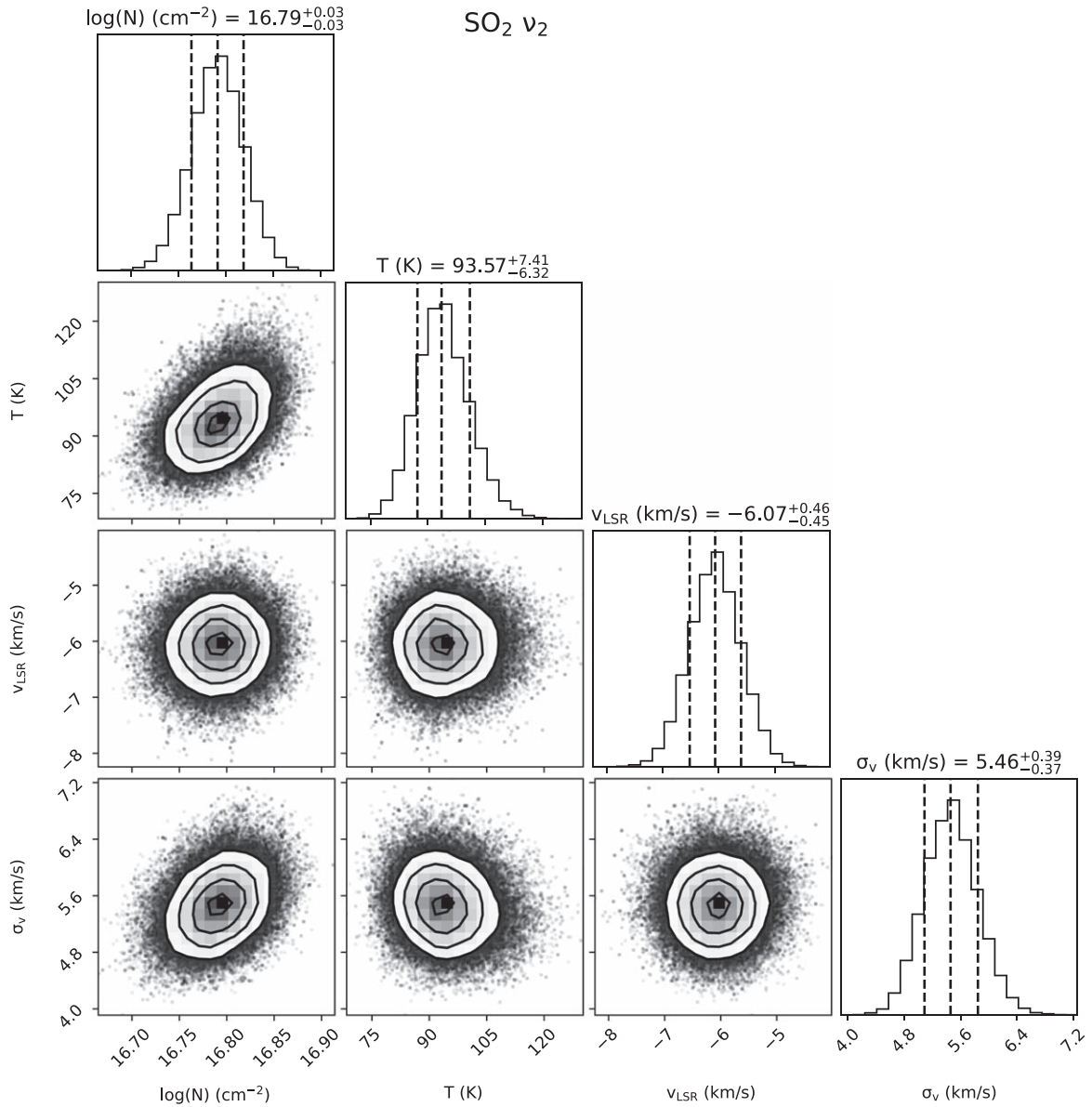
Figure 7. The posterior distribution of the log of the total column density (N), temperature (T), central LSR velocity (v_{LSR}), and line width (σ_ν) for the wavelengths dominated by SO_2 ν_2 resulting from an MCMC sampler. The left, central, and right dotted lines over the histograms correspond to the 16th, 50th, and 84th percentiles, respectively.

We compared our data to previous observations toward BN, and found that the blue clump does not extend toward BN. From ^{12}CO and ^{13}CO absorption lines covering 2–5 μm, Scoville et al. (1983) and Beuther et al. (2010) estimated the v_{LSR} of three components to be $-18/-15$, -3, and $8/9$ km s^{-1}. Further observations of H_2O with EXES at 6 μm estimate the v_{LSR} of three similar absorption components to be -17, 0.5, and 8 km s^{-1} (Indriolo et al. 2018). Though the 0.5 km s^{-1} H_2O component is quantitatively close to the v_{LSR} of the red clump, it is outside the error bars, and it is therefore unlikely that the red clump extends toward BN.

4.1.1. The Blue Clump

The blue clump has an average v_{LSR} of -7.1 ± 0.7 km s^{-1}, v_{FWHM} of 8.9 ± 1.8 km s^{-1}, and temperature of 135 ± 47 K. Every species and band observed in absorption in this survey is present in the blue clump: C_2H_2, $^{13}CCH_2$, CH_4, CS, HCN,

$H^{13}CN$, HNC, H_2O, NH_3, SO_2, and tentative OH. It has higher abundances of each species it shares in common with the red clump (C_2H_2, $^{13}CCH_2$, CH_4, and HCN), ranging from 4.19 ± 0.93 more ortho-C_2H_2 in the ν_5 band, to 1.37 ± 0.31 more para-C_2H_2 in the $\nu_4 + \nu_5$ band (Table 6). We have previously published EXES blue clump observations of C_2H_2, $^{13}CCH_2$ (Rangwala et al. 2018), HCN, $H^{13}CN$, and HNC (Nickerson et al. 2021).

Previous studies have also measured these species in absorption toward IRc2 (Evans et al. 1991; Wright et al. 2000; Boonman et al. 2003). With ISO, Wright et al. (2000) measured H_2O absorption in the MIR toward IRc2 at $v_{LSR} = -8$ km s^{-1} from 24–45 μm. These lines, except for one, are obscured in this survey by the Earth's atmosphere where coverage overlaps. The v_{FWHM} ($\approx$30 km s^{-1}) is much wider than this work's (8.9 ± 1.8 km s^{-1}), possibly because ISO's large beam included more MIR sources than just those
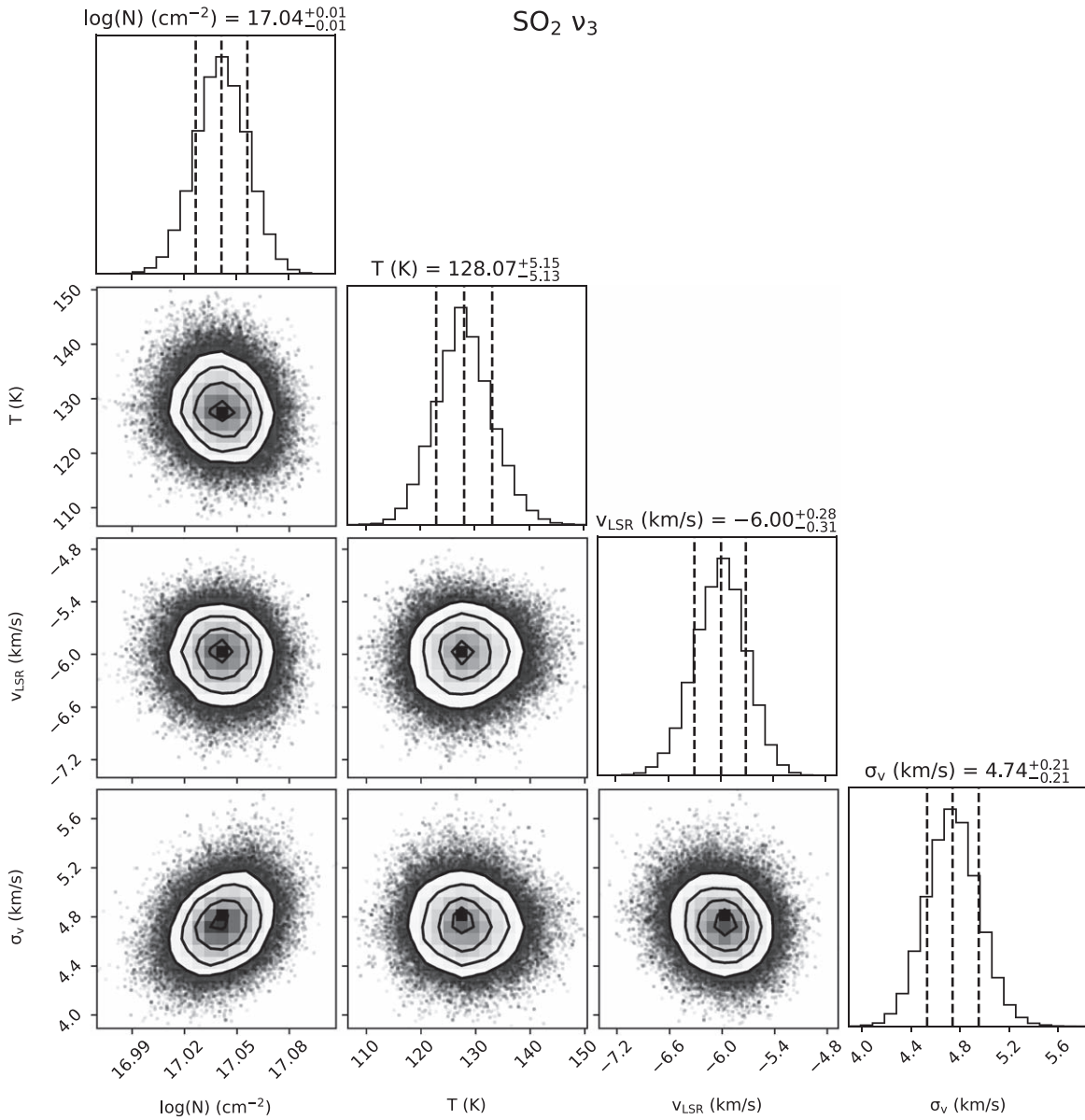
Figure 8. Similar to Figure 7, but for the wavelengths dominated by SO$_2$ ν_3.

toward IRc2 (Figure 1). In a high-resolution study toward IRc2 with IRTF/IRSHELL, Evans et al. (1991) detected the same bands of C$_2$H$_2$ (ν_5 and $\nu_4 + \nu_5$), HCN (ν_2), and NH$_3$ (ν_2) as in this work, as well as OCS (ν_1) and CO. The $v_{\rm LSR}$, however, varied widely across the species ranging from -10 km s^{-1} for CO to 7.1 km s^{-1} for C$_2$H$_2$, and was also inconsistent across multiple transitions for each individual species. This was possibly due to lower resolution and imprecise wavelength calibration. From that work, it was unclear if these species belonged to the same component. Boonman et al. (2003) analyzed the strongest ν_5 band of C$_2$H$_2$ and ν_2 band of HCN absorption features toward IRc2 with ISO, and estimated abundances comparable to hot core models and other massive protostars.

Because of EXES's higher resolution and smaller beam size, we have for the first time accurately measured the $v_{\rm LSR}$ and the $v_{\rm FWHM}$ of the blue clump consistently across several molecular species. The evidence presented here suggests that the blue clump is a distinct component that has no relationship with the classic components in the region. As laid out in Table 5, the blue clump's central velocity, line width, and temperature are distinct from these classic components as defined by previous molecular emission line surveys carried out in the submillimeter to radio wavelengths.

However, if the blue clump is related to previously studied components in the region, there are two possibilities. The first possibility is that it is part of the low-velocity flow, an outflow belonging to the plateau whose $v_{\rm LSR}$ ranges from about 8–20 km s^{-1} with respect to the ambient cloud velocity of 9 km s^{-1} (Wright et al. 1996). However, this gas is characterized by shocks, and we do not find evidence that the blue clump SO$_2$ must be formed by shocks (Section 4.2.3). The other possibility is that the blue clump is associated with the hot core in some capacity. The blue clump abundances are similar to those estimated by longer-wavelength line surveys (Table 10 in Appendix C), but the velocity of the blue clump is about 9 km s^{-1} blue-ward of the hot core. A possible scenario for the blue clump is that it may be gas that once belonged to the hot

Table 5
Overview of Kinematic Components in Orion BN/KL

Component	$v_{\rm LSR}$ (km s^{-1})	$v_{\rm FWHM}$ (km s^{-1})	T (K)	Species Detected in This Work
		MIR Components (This Work)		
Blue Clump	-7.1 ± 0.7	8.9 ± 1.8	135 ± 47	C_2H_2, $^{13}CCH_2$, CH_4, CS, HCN, $H^{13}CN$, HNC, H_2^*, H_2O, NH_3, $OH^?$, SO_2
Red Clump	1.4 ± 0.5	7.7 ± 0.5	146 ± 52	C_2H_2, $^{13}CCH_2$, CH_4, H_2^*, HCN
		[a]Classic Components (Submillimeter to Radio Surveys)		
Hot Core	[c]2.5–7.5	5–15	[b]150–400	$\cdots$
Extended Ridge	[c]7–11	3–5	55–70	$\cdots$
Compact Ridge	[c]7–9	3–5	80–150	$\cdots$
Plateau	6–9	>20	95–150	$\cdots$

Notes. Columns, from left to right, are: central local standard of rest velocity, line FWHM, temperature, and species detected in this work only. Numbers are averages for the present work, and a typical range from other works. H_2, H_2O, OH, and $2\nu_2$ HCN are not counted toward the average $v_{\rm LSR}$ and $v_{\rm FWHM}$ in this work due to only one or two lines analyzed per species. ∗ denotes emission lines. ? denotes the tentative detection of OH.
[a] Ranges are compiled from combining Blake et al. (1987), Genzel & Stutzki (1989), Tercero et al. (2010, 2011), and Esplugues et al. (2013) with supplementary data from:
[b] Wilson et al. (2000) and
[c] Wright et al. (1996).

Table 6
Column Density Ratio for Blue and Red Clumps

Species	Band	$N_{\rm blue\ clump}/N_{\rm red\ clump}$
ortho-C_2H_2	ν_5	4.19 ± 0.93
para-C_2H_2	ν_5	3.98 ± 0.88
$^{13}CCH_2$	ν_5	3.80 ± 0.45
ortho-C_2H_2	$\nu_4 + \nu_5$	1.77 ± 0.50
para-C_2H_2	$\nu_4 + \nu_5$	1.37 ± 0.31
CH_4	ν_4	2.26 ± 0.56
HCN	ν_2	2.91 ± 0.65

core (Boonman et al. 2003), separated by either outflows from Source I or the explosive event that tore the region apart 500 yr ago (Bally et al. 2017), and it has cooled from former higher hot core temperatures. Regardless of the blue clump's membership with the hot core, its high abundances means that it mimics a hot core-like chemistry with lower temperatures.

4.1.2. The Red Clump

The red clump is unique to this EXES survey, having been undetected in previously published MIR studies with other instruments. The red clump has an average $v_{\rm LSR}$ of 1.4 ± 0.5 km s^{-1}, $v_{\rm FWHM}$ of 7.7 ± 0.5 km s^{-1}, and temperature of 146 ± 52 K, within error of the blue clump. It has lower relative column densities of each species shared with the blue clump (Table 6). The red clump HCN was first reported in Nickerson et al. (2021), and in this survey, we find more molecules in the red clump: C_2H_2 (both ν_5 and $\nu_4 + \nu_5$), $^{13}CCH_2$, and CH_4. HCN and C_2H_2 on average have higher temperatures observed toward the red clump compared to the blue clump, while $^{13}CCH_2$ and CH_4 have lower temperatures. CH_4 in particular, however, is difficult to measure due to atmospheric interference, and its temperatures have large errors.

The five absorption species that we detect in the blue clump, but not in the red clump are: CS, $H^{13}CN$, HNC, NH_3, and SO_2 (our one H_2O line and tentative OH detection are not enough to comment on with regard to the red clump). Of those, HNC and both SO_2 bands have line widths ($\approx$10 km s^{-1}) much wider

compared to the blue clump species that have separate and resolved red clump components. Rangwala et al. (2018) observed a subset of the HCN and C_2H_2 transitions with EXES, but they only resolved the blue clump component with line widths >9 km s^{-1}, due to a lower integration time. In this work with the same transitions, we are able to resolve the two components, and the line widths for each species are smaller. This indicates that HNC and SO_2 may have an unresolved red clump component.

CS lines have small enough widths that there could be no measurable red clump component in this survey, while the $H^{13}CN$ lines are faint enough that its red clump component is not abundant enough for us to measure. This NH_3 data was taken with a different instrument, TEXES, than the other molecules. Unpublished TEXES archival data includes a small subset of the C_2H_2 and HCN transitions present in this survey. We found that their line shapes are identical to the two-component double Gaussians published in this survey, meaning that TEXES is capable of resolving the red clump (also see Figure 7 in Lacy et al. 2002). On the other hand, the TEXES NH_3 observations had different beam centers compared to the EXES observations, which can affect the molecular line widths in the region. It is inconclusive whether NH_3 is measurable in the red clump or not.

The red clump may, as we suggest for the blue clump, be independent of the region's classic components and is entirely new to this work. The results of analysis show that the central velocity, line width, and temperature do not neatly match any of these classic components (Table 5). The red clump is especially distinct from the extended ridge, compact ridge, and plateau.

The classic component that the red clump is possibly be related to is the hot core. It could be the hot core's outer edge as probed by IRc2 (Figure 1), exhibiting lower column densities and temperatures. In VLA radio maps, the column density of NH_3 at the line of sight toward IRc2 is $30\% \pm 10\%$ the column density toward the NH_3 peak of the hot core (Genzel et al. 1982; Wynn-Williams et al. 1984). The red clump's $v_{\rm FWHM}$ is within the hot core's range as measured by emission lines at longer wavelengths (Table 5), while its temperature falls on the
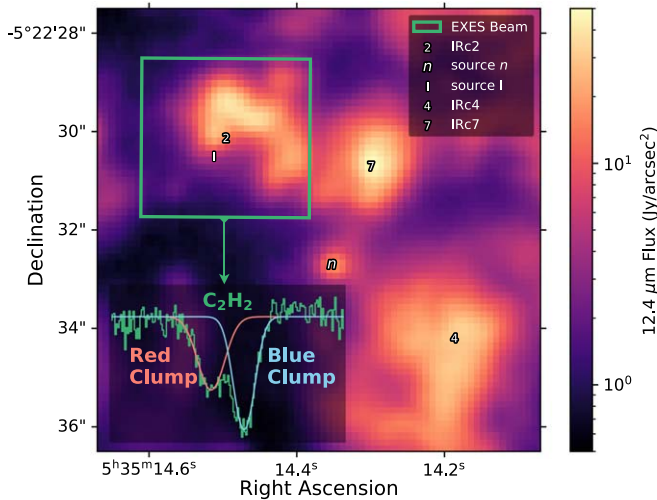
Figure 9. Close-up of the IRc2 region from Figure 1. The C_2H_2 transition ($\nu_4 + \nu_5$ band, P8) clearly has two components, the red clump and the blue clump, as also seen in other species. The color map is the 12.4 μm flux (SUBARU/COMICS; Okumura et al. 2011). The green box is the EXES beam for the 7.6a μm setting. The symbols refer to regional features discussed in this work and are placed as described in Figure 1.

Table 7
C_2H_2 Ortho-to-Para Column Density Ratios toward IRc2

Band	Blue Clump	Red Clump
ν_5	1.22 ± 0.19	1.16 ± 0.31
$\nu_4 + \nu_5$	2.45 ± 0.67	1.89 ± 0.45

cooler end of the range. However, the red clump's v_{LSR} is about 1 km s^{-1} blue-ward of the lower limit of the hot core's.

4.2. Individual Species

4.2.1. C_2H and $^{13}CCH_2$

For a detailed introduction on C_2H_2, refer to Rangwala et al. (2018). The blue clump C_2H_2 has been observed toward IRc2 with the ground-based NASA IRTF (Lacy et al. 1989; Evans et al. 1991; Carr et al. 1995) and space-based ISO (van Dishoeck et al. 1998; Boonman et al. 2003) observatories. In higher resolution, Lacy et al. (2002) presented the C_2H_2 R7 ν_5 line with TEXES, and Rangwala et al. (2018) presented C_2H_2 R8 to R17 ν_5 and $^{13}CCH_2$ R9, R10, and R12 with EXES. Note that the Rangwala et al. (2018) SOFIA/EXES observations were centered over the 13 μm peak, which could lead to slight differences in line profiles between the observations in Rangwala et al. (2018) and the present work. Furthermore, their integration time was lower than this survey's, likely explaining why they did not detect the red clump component.

This present work expands on Rangwala et al. (2018). Here we resolve C_2H_2 into two components, the blue and red clumps. For the ν_5 band of C_2H_2, we detect both ortho and para transitions in the R, P, and Q branches, and we also detect ν_5 $^{13}CCH_2$ P- and R-branch transitions. For $\nu_4 + \nu_5$ C_2H_2, we detect ortho and para P as well as para R-branch transitions. We should also note that we observe the R17e and R19e transitions in the 7.3 μm settings, but they are mixed with SO_2 lines and omitted from the analysis.

We expect that the ortho-to-para ratio (OPR) of C_2H_2 will follow similar trends as H_2. ^{12}C has a nuclear spin of zero, which means that the degeneracy of the nuclear spin wave function is 1. Thus for C_2H_2, the carbon atoms do not contribute to the spin degeneracy. The ortho and para states arise solely from the H_2 part of this linear molecular, and thus C_2H_2 is expected to exhibit the following trends with H_2. The OPR of H_2 in LTE with temperatures $\gtrsim$200 K converges to 3. The OPR for H_2 upon formation on dust grains is also 3 (Takahashi 2001; Gavilan et al. 2012), while in the cold gas of

protostellar cores and star-forming regions, H_2 is mostly in para form with OPRs <0.001 (Troscompt et al. 2009; Pagani et al. 2013; Lupi et al. 2021).

For both bands of C_2H_2 toward IRc2, the ortho- and para-C_2H_2 ladders are not in equilibrium, tracing separate temperatures and column densities (Figures 4 and 5; Table 2), as was found in Rangwala et al. (2018). Table 7 gives the OPR for both bands and velocity components. For the ν_5 band, we find a similar ratio in the blue and red clumps, 1.22 ± 0.19 and 1.16 ± 0.31, respectively. This is similar to the result in Rangwala et al. (2018), 1.7 ± 0.1 in the blue clump. The OPR in the $\nu_4 + \nu_5$ band is closer to the equilibrium value of 3 in the blue and red clumps, 2.45 ± 0.67 and 1.89 ± 0.45, respectively. This indicates that the $\nu_4 + \nu_5$ band is located in a physically different region that is approaching equilibrium.

This survey's values for OPR in both components are much closer to the formation value of 3 than that found in cold, star-forming gas. This may reflect the recent liberation of molecules with a high OPR from dust grains into the gas phase by shocks (Rangwala et al. 2018) or protostellar heating (Dickens & Irvine 1999).

In the blue clump, the ortho ladder is systematically tracing hotter gas for both bands (ν_5 has 175 ± 12 K for ortho and 145 ± 9 K for para; $\nu_4 + \nu_5$ has 124 ± 13 for ortho and 73 ± 14 K for para). In the red clump, the ortho ladder traces hotter gas in ν_5 (229 ± 27 K for ortho and 158 ± 16 K for para) and cooler gas in $\nu_4 + \nu_5$ (111 ± 14 K for ortho and 140 ± 18 K for para).

Toward the hot cores AFGL 2591 and 2136, with EXES, Barr et al. (2020) measured an C_2H_2 OPR of $\approx$2 and attribute this lower value to optical depth effects. We do not see evidence of optically thick lines in our own data and have found other explanations, though we cannot rule out this possibility.

We discuss the isotope ratio $^{12}C/^{13}C$ in Section 4.3 and the band ratio $N_{\nu_4+\nu_5}/N_{\nu_5}$ in Section 4.4.

4.2.2. CH_4

CH_4 is among the simplest organic molecules and, along with C_2H_2, gas-phase CH_4 is an important carbon reservoir (Markwick et al. 2000; Aikawa et al. 2008). Its detection remains scarce in astrochemical surveys because its lack of a permanent dipole moment dictates that its transitions are not accessible at longer wavelengths. Due to its presence in Earth's atmosphere, it is only accessible from space or the ground in objects with a high Doppler shift. Experimental (Qasim et al. 2020), observational (Lacy et al. 1991; Boogert et al. 1998, 2004; Öberg et al. 2008), and modeling (Hasegawa et al. 1992) studies suggest that CH_4 forms from the hydrogenation of carbon atoms on dust grains in the polar (i.e., H_2O-rich) ices of dark molecular clouds. Evolving protostars then heat their natal cloud and sublimate CH_4 from the solid- into the gas-phase (Boogert et al. 2004) at 90 K (Tielens & Whittet 1997).

CH$_4$ has been observed in both the solid and gas phases toward the hot cores W3, W33A, NGC 7538 IRS 1 and 9, and AFGL 2591 (Lacy et al. 1991; Boogert et al. 1996, 1998, 2004; Carr et al. 1995; Knez et al. 2009; Barentine & Lacy 2012). Ground-based spectroscopy with IRSHELL first tentatively detected the R-branch CH$_4$ ν_4 toward Orion IRc2 (Lacy et al. 1991). Later, ISO observed gas-phase Q-branch CH$_4$ ν_2/ν_4 at 7.66 μm in emission toward IRc2, but did not resolve individual lines (van Dishoeck et al. 1998).

We measure one Q-branch and five R-branch lines of the ν_4 band of CH$_4$ in both the blue and red clumps. The 7.68 μm solid CH$_4$ transition feature found toward other hot cores (Boogert et al. 1997) is not present in this survey due to strong atmospheric interference. We also do not observe the 7.66 μm gas-phase emission feature (van Dishoeck et al. 1998), likely because ISO's beam size is much larger than EXES and the feature they found may originate from elsewhere in the region.

The temperatures of the gas-phase CH$_4$ in both the blue and red clumps (193 ± 42 and 141 ± 33 K, respectively) are higher compared to the hot cores NGC 7538 IRS 9 (55–70K) and W33A (110 K; Boogert et al. 1998, 2004). This suggests that the blue and red clumps had a stronger heating source, liberating more CH$_4$ into the gas phase. This is despite the fact that W33A and NGC 7538 IRS 9 are conventional hot cores with embedded massive protostars (Capps et al. 1987; Campbell & Persson 1988; Mitchell et al. 1990), while the Orion hot core region and IRc2 itself are externally heated. CH$_4$ is hotter toward NGC 7538 IRS 1 ($\approx$670 K; Knez et al. 2009) compared to this survey, however, which is suitable given that NGC 7538 IRS 1 has an evolved embedded protostar (Campbell & Persson 1988; Knez et al. 2009).

4.2.3. CS and SO$_2$

H$_2$S is a likely candidate for the dominant sulfur reservoir in the icy mantles of dark clouds (Charnley 1997; Hatchell et al. 1998; Wakelam et al. 2004; Woods et al. 2015; Vidal & Wakelam 2018), while alternative suggestions include OCS (Charnley 1997; van der Tak et al. 2003), atomic sulfur, and HS (Vidal & Wakelam 2018). As protostars heat up the ice grains in hot core regions, these reservoir species evaporate, and subsequent reactions produce sulfur molecules, including CS and SO$_2$.

Shocks enhance SO$_2$ abundances, making SO$_2$ a typical tracer of shocked gas (Hartquist et al. 1980; des Forets et al. 1993; Bachiller & Gutiérrez 1997; Burkhardt et al. 2019). In a radio survey of the Orion BN/KL region, Esplugues et al. (2013) identified SO$_2$ emission as an excellent tracer of shocked gas in the plateau and warm, dense gas in the hot core. Blake et al. (1987) also associated the plateau with high-velocity shocked gas, while Charnley (1997) found no evidence of shock chemistry in the hot core.

We have observed the ν_2 and ν_3 bands of SO$_2$ toward IRc2 in the blue clump only. The velocities of both bands (-6.1 ± 0.5 km s^{-1} and -6.0 ± 0.3 km s^{-1}, respectively) are somewhat red-ward of the other blue clump species. The SO$_2$ line widths are much narrower than those of the plateau shocked gas (Table 5). The line widths of both bands ($\approx$12 km s^{-1}) are slightly larger than the blue clump's average (8.9 ± 1.8 km s^{-1}) but are similar to the line widths of HNC, and, as discussed in Section 4.1.2, may be wide due to an unresolved red clump component. Therefore, we attribute this survey's SO$_2$ to the blue clump and not shocked plateau gas.

The temperatures we measure, $\approx$100 K, are high enough to form SO$_2$ from hot core-like chemistry, typically 50–300 K in models (Charnley 1997; Hatchell et al. 1998; Wakelam et al. 2004). The SO$_2$ therefore likely arose by liberation from icy dust grains as the blue clump heated up, along with the other molecules we observe, and not shock chemistry.

At least six other hot cores do not have shock signatures associated with SO$_2$ (Keane et al. 2004; Dungee et al. 2018). Toward Orion IRc2 itself, ISO observed ν_3 SO$_2$ in emission (van Dishoeck et al. 1998), while we observe the same band in absorption. This difference is likely because ISO's larger beam measured the SO$_2$ emission from a region other than IRc2.

Submillimeter to radio observations of sulfur-bearing molecules in hot cores and molecular clouds have found a sulfur deficit several orders of magnitude lower than solar sulfur abundance (Charnley 1997; Tieftrunk et al. 1994; Herpin et al. 2009; Woods et al. 2015). One possible solution is that these wavelengths do not probe the hottest, inner regions of hot cores where more sulfur has evaporated into the gaseous phase (Tieftrunk et al. 1994; Herpin et al. 2009). MIR observations can, however, probe these regions. The $\nu = 1 - 0$ band of CS has been detected in the MIR toward the hot cores NGC 7538 IRS 1 (Knez et al. 2009), AFGL 2136, and AFGL 2591 (Barr et al. 2018, 2020), with abundances 2–3 orders of magnitude higher than submillimeter to radio observations of the same hot cores.

Toward Orion IRc2, we observe the $\nu = 1-0$ band's R branch of CS in the blue clump with a temperature 175 ± 34 K. The CS abundance, $(3.67 \pm 2.15) \times 10^{-8}$, falls within the range measured from FIR–radio emission lines of the Orion hot core, 2.90×10^{-9} to 1.4×10^{-7} (Sutton et al. 1995; Persson et al. 2007; Tercero et al. 2010; Crockett et al. 2014; see Table 10 in Appendix C). Similarly, the SO$_2$ abundances in each band ($(3.25 \pm 1.89) \times 10^{-7}$ for ν_2 and $(5.79 \pm 3.36) \times 10^{-7}$ for ν_3) are close to the upper limit of longer-wavelength observations of the hot core, 4.7×10^{-8} to 6.2×10^{-7} (Sutton et al. 1995; Crockett et al. 2014; Gong et al. 2015; Feng et al. 2016; Luo et al. 2019, see Table 10). It appears, at least where SO$_2$ and CS are concerned, that the MIR measurements toward IRc2 do not uncover a repository of missing sulfur. The missing sulfur may still be hiding at infrared wavelengths, but in yet-to-be detected species (Bilalbegović & Baranović 2015).

For a discussion on the ratio of the SO$_2$ ν_2 and ν_3 bands, refer to Section 4.4.

4.2.4. H$_2$

H$_2$, being the most abundant molecule in the universe, is the main species from which molecular gas is composed. It is an important coolant of the interstellar medium (Gnedin & Kravtsov 2011), and its presence is strongly correlated with star formation (e.g., Leroy et al. 2013). However, it is difficult to detect directly. Its lack of a dipole moment limits its available transitions to FIR wavelengths and shorter (Bolatto et al. 2013), with strong transitions starting in the MIR. Cooler H$_2$ may be observed in absorption against a background ultraviolet source, while the infrared is critical to detecting H$_2$ in high-temperature environments (Wakelam et al. 2017).

In the Orion region, H$_2$ emission has been directly measured in both the near- and mid-IR (Beckwith et al. 1978; Beck 1984; Brand et al. 1989; Parmar et al. 1994; Burton & Haas 1997; Rosenthal et al. 2000; Allers et al. 2005). Toward IRc2 in

particular, ISO detected the H_2 pure rotational transitions from S(0) to S(17) (van Dishoeck et al. 1998). However, given ISO's large beam size, further localization of the H_2 gas was not possible.

In this survey, we detected the S(1) pure rotational H_2 transition at 17.03 μm in emission. Similar to the survey's absorption lines, our H_2 emission line fits to a double Gaussian. The v_{LSR} of each H_2 component, -10.7 ± 2.6 and 0.5 ± 0.5 km s^{-1}, is within the error close to the average v_{LSR} of the blue and red clumps, respectively (Table 5). Thus, our H_2 emission is likely associated with the same gas as the blue and red clumps. We note that the v_{FWHM} of each H_2 component is wider than that of the absorption lines, especially in the blue clump.

Our observation of the H_2 S(1) transition in both the red and blue clumps supports our conclusion that these could be two unique components that are independent of the classic components in the region previously measured by molecular emission line surveys at longer wavelengths.

Because we cannot measure N_{H_2} from a single line, we choose a range $N_{H_2} = (1.9 \pm 1.1) \times 10^{23}$ cm^{-2}, as estimated by Evans et al. (1991) in the line of sight toward Orion IRc2 to calculate the abundances (Table 3, discussed in Section 3.2). As discussed in Section 4.1, the blue and red clumps may or may not be associated with the hot core itself. Given that we cannot conclusively match the blue and red clumps to other components in the region found at longer wavelengths, the Evans et al. (1991) value is the best option. We do note the large uncertainty for finding N_{H_2} in this region. Estimations for the hot core alone range between 10^{23} and 5×10^{24} cm^{-2} (Blake et al. 1987; Schilke et al. 1992; Sutton et al. 1995; Persson et al. 2007; Tercero et al. 2010; Favre et al. 2011; Plume et al. 2012; Crockett et al. 2014; Hirota et al. 2015; Feng et al. 2016; Peng et al. 2019).

We do not observe the H_2 S(0) transition at 28.22 μm even though this region is covered by this survey's 28.1 μm setting. Assuming the same v_{LSR} as S(1), S(0) falls into an atmosphere-free region of the spectrum. S(0) is intrinsically weaker by an order of magnitude compared to S(1), and IRc2 is much brighter at the longer wavelengths, requiring a higher continuum signal-to-noise than achieved, both of which can explain this line's absence. The other H_2 transitions fell outside of this survey's coverage.

The Orion BN/KL region hosts several H_2 "bullets" as detected by the $\nu = 1$–0 S(1) transition at 2.121 μm, caused by the explosive event that occurred about 500 yr ago (Nissen et al. 2007, 2012). However, most of IRc2, especially our beam center, does not probe these H_2 structures. It is therefore unlikely that the H_2 in this work, as well as the blue and red clumps, are associated with these bullets.

4.2.5. H_2O

We observe one well-defined H_2O absorption line in the wings of an atmospheric line (Figure 10, upper-left panel): a pure rotational transition, 5_{41}–4_{14}, at 25.9 μm. This line was previously also observed by Wright et al. (2000) toward IRc2 with ISO, one of 19 pure rotational lines. That work observed two other lines covered by this survey, but we do not observe them, as they are obscured by the atmosphere. We also observe a bump corresponding to the 7_{44}–6_{15} transition at 26.0 μm that was not separated enough from the atmosphere to analyze. This transition was not seen in Wright et al. (2000).

After dividing out the atmosphere, we fit 5_{41}–4_{14} to a Gaussian to obtain a rough estimate of the $v_{LSR} = -8.0 \pm 0.4$ km s^{-1}, which fits with the blue clump component. The $v_{FWHM} = 17.0 \pm 1.0$ km s^{-1} is much wider than all other absorption lines in this survey. It may be an artifact of being blended with the atmosphere. If it is in fact real, there are two possible explanations. First, that H_2O is much more abundant compared to the other molecular species and the line is broadened by saturation. Second, that the larger solid angle of the brighter continuum at 26 μm causes us to observe molecules at more positions in the beam with slightly different central velocities. We did find that extracting only the interior 2.″5 of the slit results in a narrower line.

Our H_2O observations were possible for the 25.3 through 28.1 μm settings due to the Doppler shift in March, while the observation of any water absorption was impossible for the 16.3–24.7 μm settings taken in October.

We also observe numerous ν_2-band H_2O emission lines in the 7.3–7.9 μm settings, all in the P branch. Their average $v_{LSR} = 8.8 \pm 0.1$ km s^{-1} places them in a region that is similar to the SiO emission lines and they are separate from the absorption lines in the blue and red clumps. A future publication will provide a detailed analysis and treatment of the H_2O emission.

4.2.6. HCN, H^{13}CN, and HNC

Nickerson et al. (2021) covered the species HCN, H^{13}CN, and HNC in detail but here we summarize the results. They measured the P-, Q-, and R-branch transitions of HCN and HNC, as well as the R-branch transitions of H^{13}CN, all in the ν_2 band. The blue clump hosts all three species, while only HCN has a clear red clump component. In the blue clump, they derived HCN/HNC $= 72 \pm 7$, in line with submillimeter to radio measurements of the region. With chemical network modeling (Acharyya & Herbst 2018), they found that the gas reaches this ratio after 10^6 yr. This suggests that the blue clump may predate the explosive event in the region that occurred 500 yr ago (Bally et al. 2011). In Section 4.3 we discuss the isotope ratio ^{12}C/^{13}C.

Note that the temperatures and column densities resulting from rotation diagram analysis in Nickerson et al. (2021) differed from those reported here, because in the previous work, individual branches were fit, while here we fit all branches in a single species together (Table 2). The difference is only noteworthy for red clump HCN, where fitting all branches together results in a lower temperature. This did not affect the HCN/HNC column density ratio. Also, the nomenclature is different in Nickerson et al. (2021) in which they referred to the blue clump as the primary velocity component and the red clump as the secondary velocity component. They chose a different value for N_{H_2} in Nickerson et al. (2021) than in this work, an Atacama Large Millimeter/submillimeter Array measurement toward the hot core (Peng et al. 2019), while here in Table 3 we use an estimation toward Orion IRc2 itself (Evans et al. 1991).

New to this work, we report the detection of five $2\nu_2$ HCN lines in the 7.3 μm setting, P10e to P14e. Due to the forest of SO$_2$ lines in this setting, it is difficult to measure other species. We divide the setting by the simulated SO$_2$ spectra (Section 3.3) and satisfactorily fit P10e and P12e to double Gaussians with central velocities close to the blue and red clumps. The other three lines were mixed with atmospheric and

deep SO_2 lines. The spectral region after division was not robust enough to fit. With only two lines fit, we do not have enough data points to draw a reliable rotation diagram and estimate the temperature and the column density of $2\nu_2$ HCN with confidence.

4.2.7. NH₃

NH₃ is a commonly used tracer of gas temperature in star-forming regions (Ho & Townes 1983). Previous measurements of NH₃ in the region have been conducted mostly in radio, and limited to emission lines. Radio mapping of NH₃ in the Orion BN/KL region showed that NH₃ emission lines peak toward the hot core (Ho et al. 1979; Murata et al. 1990; Wilson et al. 2000; Goddi et al. 2011; Friedel & Looney 2017) and pinpoint source I as the main heating source of the hot core (Wilson et al. 2000; Goddi et al. 2011). Rotation diagrams of the hot core NH₃ reveal two temperature components in radio, 130 K for transitions <1000 K, and 400 K for higher-energy transitions (Hermsen et al. 1988; Wilson et al. 1993, 2000).

In the TEXES spectra, we observe five P-branch NH₃ transitions in the ν_2 band, two para and three ortho, in the blue clump. They were not numerous enough to fit to separate ortho and para rotation diagrams, and we fit all five lines as a single species. This is reasonable, however, because at temperatures over 30 K, NH₃ that has formed via gas-phase reactions is expected to have an OPR of 1. Radio NH₃ mapping of the Orion hot core shows an OPR of 0.9–1.6 (Goddi et al. 2011). Elsewhere, TEXES observations of the hot cores AFGL 2591 and 2136 (Barr et al. 2020) fit ortho- and para-NH₃ to separate rotation diagrams, but find that they both agree on temperature and column density.

Toward Orion IRc2 we obtain a temperature of 230 ± 86 K, which falls into the spread of hot core temperatures measured in FIR to radio from 118–400 K (Hermsen et al. 1988; Wilson et al. 1993, 2000; Crockett et al. 2014; Gong et al. 2015; Friedel & Looney 2017). The abundance ($(8.32 \pm 6.29) \times 10^{-8}$; Table 3) is close to the lower limit of hot core measurements at longer wavelengths, $(4.0 \pm 2.1) \times 10^{-7}$–$(6.0 \pm 3.5) \times 10^{-6}$ (Persson et al. 2007; Gong et al. 2015; see Table 10 in Appendix C). This fits with the possibility discussed in Section 4.1.1 that the blue clump may exhibit hot core-like chemistry.

4.2.8. OH

OH is important to the formation of water (e.g., Keto et al. 2014). We observe a tentative OH line from the two pure rotational R(7/2) transitions at 24.6417 and 24.6419 μm. The two transitions are close enough to be blended into a doublet, and we estimate $v_{LSR} \approx -8$ km s^{-1}, situating it in the blue clump. There are other strong transitions covered by the 24.7–28.1 μm settings, but at the typical temperatures of the other blue clump molecules ($\approx$100–200 K), these transitions are weaker than the observed doublet. Another strong transition pair falls between orders.

Previously in the MIR with ISO SWS, Wright et al. (2000) observed three pure rotational OH absoprtion lines from 28.93 to 34.62 μm, which is beyond our survey's coverage. In the FIR, Lerate et al. (2006) detected OH with ISO LWS toward IRc2 largely attributed to the plateau. They found absorption and P-Cygni lines at shorter wavelengths and emission lines at longer wavelengths.

4.2.9. SiO

We detect several $\nu = 1$–0 band SiO emission lines with an average $v_{LSR} = 9.8 \pm 0.1$ km s^{-1} in the R branch. This is a similar velocity to the H_2O emission and is different than the blue and red clumps, in which we observe the absorption lines and H_2 emission. A future publication will provide a detailed analysis for the SiO lines.

4.2.10. [Fe II], [Ne II], [S I], and [S III]

Forbidden line emission from [Ne II] (12.81 μm), [S III] (18.71 μm), [S I] (25.25 microns), and [Fe II] (25.99 μm) are measured at the off-source position and, except for [Fe II], at the on-source position toward IRc2.

The line brightnesses are consistent with ISO (Rosenthal et al. 2000) and Spitzer measurements (position I4 of Rubin et al. 2011, which is at the most similar distance from from the ionizing star theta 1C as are our two positions), though both studies averaged over much larger areas. The agreement with larger area measurements and the detection of emission at both the on- and off-source positions indicates that the EXES spectra are sampling extended emission.

Ne^+ and S^{++} require 22 eV photons, and the [Ne II] and [S III] lines have slightly blueshifted LSR velocities, so this emission probably originates from the extended Huygen's region of the Orion Nebula (O'Dell et al. 2020), where hydrogen is fully ionized. The [S I] and [Fe II] lines have similar, redshifted LSR velocities at the off-source position where both are detected. Based on the velocities and the extended emission, these lines likely originate from the photodissoication region lying behind the Huygen's region, between it and OMC-1 (e.g., O'Dell et al. 2017).

4.3. $^{12}C/^{13}C$

For C_2H_2, we find $^{12}C/^{13}C = 21.3 \pm 2.2$ and 19.8 ± 3.4 in the blue and red clumps, and for HCN, 12.5 ± 2.1 in the blue clump (Table 8). This is similar to the original C_2H_2 blue clump measurement in Rangwala et al. (2018), 14 ± 1.

Nickerson et al. (2021) discussed this ratio in detail in the context of HCN, providing a comparison between the ratio we find and those at longer wavelengths. By Galactocentric distance, this ratio is expected to be 50–90 (Favre et al. 2014; Milam et al. 2005). Submillimeter to radio studies toward IRc2 have measured $^{12}C/^{13}C = 20$ to 79.6 (Schilke et al. 1997; Tercero et al. 2010; Favre et al. 2014; Feng et al. 2016), and we match the lower end of those measurements. EXES's small beam size in the MIR means that we are able to probe different gas compared to these previous measurements. Another possible explanation for this low ratio is that the HCN and C_2H_2 lines are optically thick. However, the lines do not display flat bottoms, a typical sign of optical thickness.

Other star-forming regions have reported a lower $^{12}C/^{13}C$ compared to expectations based on Galactocentric distance (Daniel et al. 2013; Jørgensen et al. 2018; Magalhães et al. 2018) as well as planetary nebulae (Ziurys et al. 2020). This may hint at new chemical processes (Colzi et al. 2020). Ultimately, we require more measurements of this isotope toward hot cores in the MIR in order to determine if these results are an anomaly or part of a wider trend.

Table 8
^{12}C/^{13}C Column Density Ratios

Species	Blue Clump	Red Clump
C$_2$H$_2$	21.3 ± 2.2	19.8 ± 3.4
HCN	12.5 ± 2.1	⋯

Table 9
Band Column Density Ratios

Species	Band Ratio	Ladder	Blue Clump	Red Clump
C$_2$H$_2$	$\nu_4 + \nu_5/\nu_5$	Ortho	5.59 ± 1.11	13.2 ± 3.95
		Para	2.78 ± 0.68	8.09 ± 1.63
SO$_2$	ν_3/ν_2	⋯	1.78 ± 0.5	⋯

Note. The central wavelengths of species' bands: C$_2$H$_2$ $\nu_4 + \nu_5$ at 7.6 μm, C$_2$H$_2$ ν_5 at 13.5 μm, SO$_2$ ν_3 at 7.2 μm, and SO$_2$ ν_2 at 19 μm.

4.4. Band Ratios

We have column density measurements of two different bands for two species: C$_2$H$_2$ and SO$_2$. Each absorption band for these two species probe the ground state of the gas. We would expect, therefore, the same temperature and column density if they were probing the same material. The fact that the bands have different column densities and temperatures (Table 2) means that the different bands are probing different material. First, because the brightest point in the continuum of IRc2 at different wavelengths changes position, the bands probe slightly different positions in R.A. and decl. (as discussed in Section 2). Second, and perhaps more importantly, the different bands probe different depths along the line of sight. As explained below, shorter wavelengths tend to probe deeper material. This effect is also seen in the conventional hot cores AFGL 2591 and 2136 (Barr et al. 2020).

For the blue clump C$_2$H$_2$, we estimate $N_{\nu_4+\nu_5}/N_{\nu_5} = 5.59 \pm 1.11$ and 2.78 ± 0.68 for the ortho and para, respectively. We measure higher ratios in the red clump, 13.2 ± 3.95 and 8.09 ± 1.63 for ortho and para, respectively. Another way to highlight the difference is that individual quantum states of the different bands of C$_2$H$_2$ also have different column densities (e.g., P3e; see Table 11). We only measure SO$_2$ in the blue clump and find $N_{\nu_3}/N_{\nu_2} = 1.78 \pm 0.5$ (Table 9; these ratios are given with the shorter-wavelength bands in the numerator).

Toward IRc2, Evans et al. (1991; with corrections in Carr et al. 1995) previously measured this ratio for C$_2$H$_2$ in the blue clump to be $\approx$ 5–6, which is similar to this survey's numbers. The present work's more extensive measurements support the original explanation Evans et al. (1991) and Carr et al. (1995) put forth for the band ratio: emitting dust is mixed with these molecular species observed in absorption. The optical depth of dust is greater at 13.5 μm (ν_5) than at 7.6 μm ($\nu_4 + \nu_5$) (Draine 1989; though the extent of their difference depends on the model—see Xue et al. 2016). Therefore the $\nu_4 + \nu_5$ band samples gas deeper into each clump, which results in higher column densities. This effect is apparent in both the blue and red clumps, with the greater ratio in the red clump. Similarly for SO$_2$, we also find that the shorter-wavelength band, ν_3 at 7.2 μm, has a larger column density compared to the longer-wavelength band ν_2 at 19 μm, though the ratio is much lower compared to C$_2$H$_2$.

Interestingly, in both clumps the gas probed by the ν_5 band of C$_2$H$_2$ is hotter (ortho blue clump 175 ± 12 K; para blue clump 145 ± 9 K; ortho red clump 229 ± 27; para red clump 158 ± 16) than that by the $\nu_4 + \nu_5$ band (ortho blue clump 124 ± 13 K; para blue clump 73 ± 14 K; ortho red clump 111 ± 14; para red clump 140 ± 18), while the ν_3 band of SO$_2$ probes hotter gas (128 ± 5 K) than the ν_2 band (94^{+7}_{-6} K). With the evidence here, at least, it is clear that along the line of sight, we are probing different physical structure at different bands. However, we also cannot rule out that some of the differences

are caused by the changing position of the IRc2 continuum at different wavelengths.

Though we have many lines of ν_2 HCN at 13.5 μm, we only obtain two clean lines of $2\nu_2$ HCN at 7.0 μm, which is not enough for a linear fit. If we draw a line between the two points given, we obtain column densities of roughly 3×10^{17} and 5×10^{16} cm^{-2}, giving $N_{2\nu_2}/N_{\nu_2} = 6$ and 2.5 in the blue and red clumps, respectively. This agrees with the C$_2$H$_2$ and SO$_2$ measurements where the shorter-wavelength band is more abundant. We must stress, however, the highly uncertain nature of this calculation with HCN.

5. Conclusions

With SOFIA/EXES we present the first MIR survey in the Orion BN/KL region with high enough spectral resolution to resolve individual molecular transitions of multiple species from 7.2–28.3 μm. We target IRc2, the second-brightest MIR source in the region, which coincides with the outer edge of the Orion hot core (Figure 1). This work builds on publication of previous SOFIA/EXES observations of C$_2$H$_2$, ^{13}CCH$_2$, HCN, H^{13}CN, and HNC toward IRc2 (Rangwala et al. 2018; Nickerson et al. 2021). We supplement this survey with a small amount of IRTF/TEXES data around 11.8 μm, where ground-based observations are comparable to SOFIA.

Our main results are as follows:

1. For the first time, two new kinematic components in the region are unambiguously identified in the MIR with multiple species, which we refer to as the blue clump and the red clump. These two components are characterized by molecular absorption lines. Their temperatures ($\approx$140 K) and $v_{\rm FWHM}$ ($\approx$8 km s^{-1}) are similar. Their central velocities differ with -7.1 ± 0.7 km s^{-1} for the blue clump and 1.4 ± 0.5 km s^{-1} for the red clump (Table 5). The blue clump has higher column densities of each species it shares in common with the red clump, ranging from about 1.4–4.2 (Table 6). In the blue clump we detect every molecular species in absorption in this work: C$_2$H$_2$, ^{13}CCH$_2$, CH$_4$, CS, H$_2$O, HCN, H^{13}CN, HNC, NH$_3$, SO$_2$, and tentatively OH. The red clump contains a subset of these species: C$_2$H$_2$, ^{13}CCH$_2$, CH$_4$, and HCN.

2. The blue and red clumps could be their own distinct components with no relationship with the classic components previously identified in the region by emission line surveys at longer wavelengths. IRTF/TEXES (Lacy et al. 2002) and VLT/CRIRES (Beuther et al. 2010) spectra show that the blue clump is extended to cover IRc7, IRc4, and source n, while the extent of the red clump is unclear. Future MIR mapping and spectroscopy in the Orion BN/KL region could clarify the nature of the blue and red clumps.

3. We observe one pure rotational transition of H_2, S(1), in emission with two kinematic components with $v_{LSR} = -10.7 \pm 2.6$ km s^{-1} and 0.5 ± 0.5 km s^{-1}. These components fall within error of the central velocities for the blue and red clumps, respectively. It is likely that the S(1) H_2 emission traces the blue and red clumps. This supports our supposition that the blue and red clumps are independent of other regional components and future observations of H_2 in the region may help us further understand the blue and red clumps.

4. We also observe numerous H_2O and SiO lines in emission with a v_{LSR} of around 9 km s^{-1}. They belong to neither blue nor red clumps, and detailed analysis of these lines will appear in a future publication. We provided a limited analysis of the atomic forbidden transitions [Fe II], [S I], [S III], and [Ne II] observed both on-source toward IRc2, and toward the off-source position.

5. Ortho- and para-C_2H_2 are not in equilibrium, with separate temperatures and column densities (Table 7). This suggests that C_2H_2 has been recently liberated from dust grains and has little in common with the cold gas in star-forming regions. In the blue and red clumps, the ν_5 band (13.5 μm) has an OPR of 1.22 ± 0.19 and 1.16 ± 0.31, respectively, while the $\nu_4 + \nu_5$ band (7.6 μm) has an OPR of 2.45 ± 0.67 and 1.89 ± 0.45, respectively. This difference in OPR indicates that the gas traced by each band is located in physically different regions within the clumps, and the $\nu_4 + \nu_5$ band is closer to equilibrium in both clumps.

6. With HCN and H^{13}CN in the blue clump and C_2H_2 and ^{13}CCH$_2$ in both clumps, we find ^{12}C/^{13}C $\approx$ 10–20 in both clumps. This is much lower than what is expected given the Galactocentric distance of Orion BN/KL.

7. Numerous lines are observed in two different bands at two different wavelengths for C_2H_2 (blue and red clumps) and SO_2 (blue clump only). The ratio of column densities of these bands reveals that in both clumps, the shorter-wavelength band has the higher column density. This suggests that shorter wavelengths probe material deeper into the clumps along the line of sight.

Our survey highlights the importance of the MIR. While the Orion BN/KL region is the closest and best-studied massive star-forming region, a paucity of MIR observations has left much unobserved until this work. The MIR provides an observational window to rovibrational transitions and many molecules, including C_2H_2, CH_4, and H_2, that lack a permanent dipole moment. In this survey the MIR probes kinematic components not visible to longer wavelengths. The fact that the blue and red clumps have different abundances despite having similar temperatures and line widths suggests that they have followed separate paths of chemical evolution. Further MIR observations in the region, along with testing chemical networks against this survey's results, will broaden our understanding of the unique molecular inventory presented in this work.

Appendix A
Gallery of Observed Spectral Lines

Figures 10–13 show examples of normalized EXES flux with the atmospheric models. Figures 10–12 give examples of each molecule detected towards Orion IRc2. Figure 12 additonally shows synthetic models of SO_2 spectra. Figure 13 shows all four atmoic and ion lines detected towards Orion IRc2.
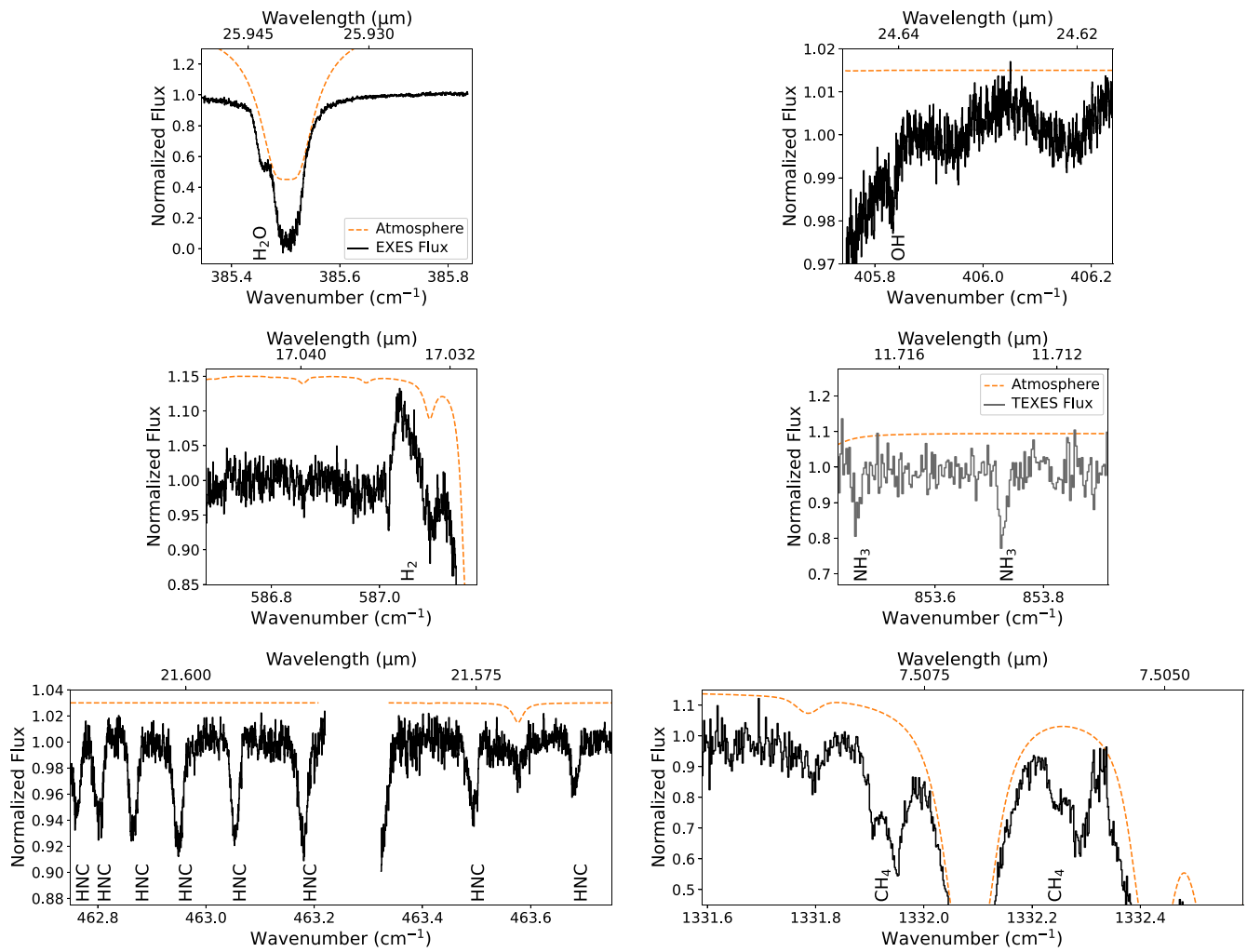
Figure 10. Examples of molecular transition lines observed with SOFIA/EXES (solid black) and TEXES (solid gray) with offset atmospheric transmission (dotted orange). Species left to right, top to bottom: H_2O; OH (gray); H_2; NH_3; HNC; and CH_4.
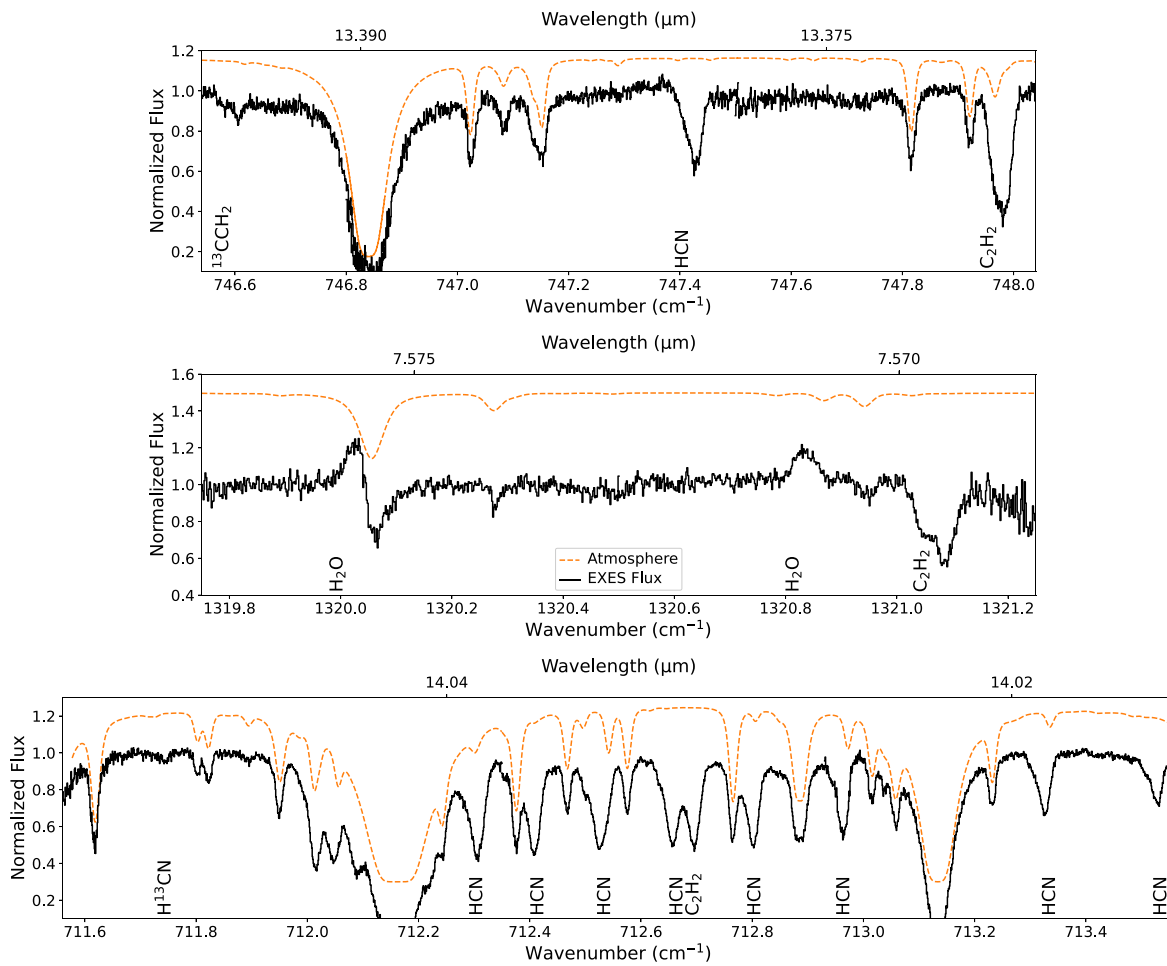
Figure 11. Examples of molecular transition lines observed with SOFIA/EXES (solid black) with offset atmospheric transmission (dotted orange). Species top to bottom: $^{13}CCH_2$, HCN, and the ν_5 band of C_2H_2; H_2O and the $\nu_4 + \nu_5$ band of C_2H_2; and $H^{13}CN$, HCN, and the ν_5 band of C_2H_2.
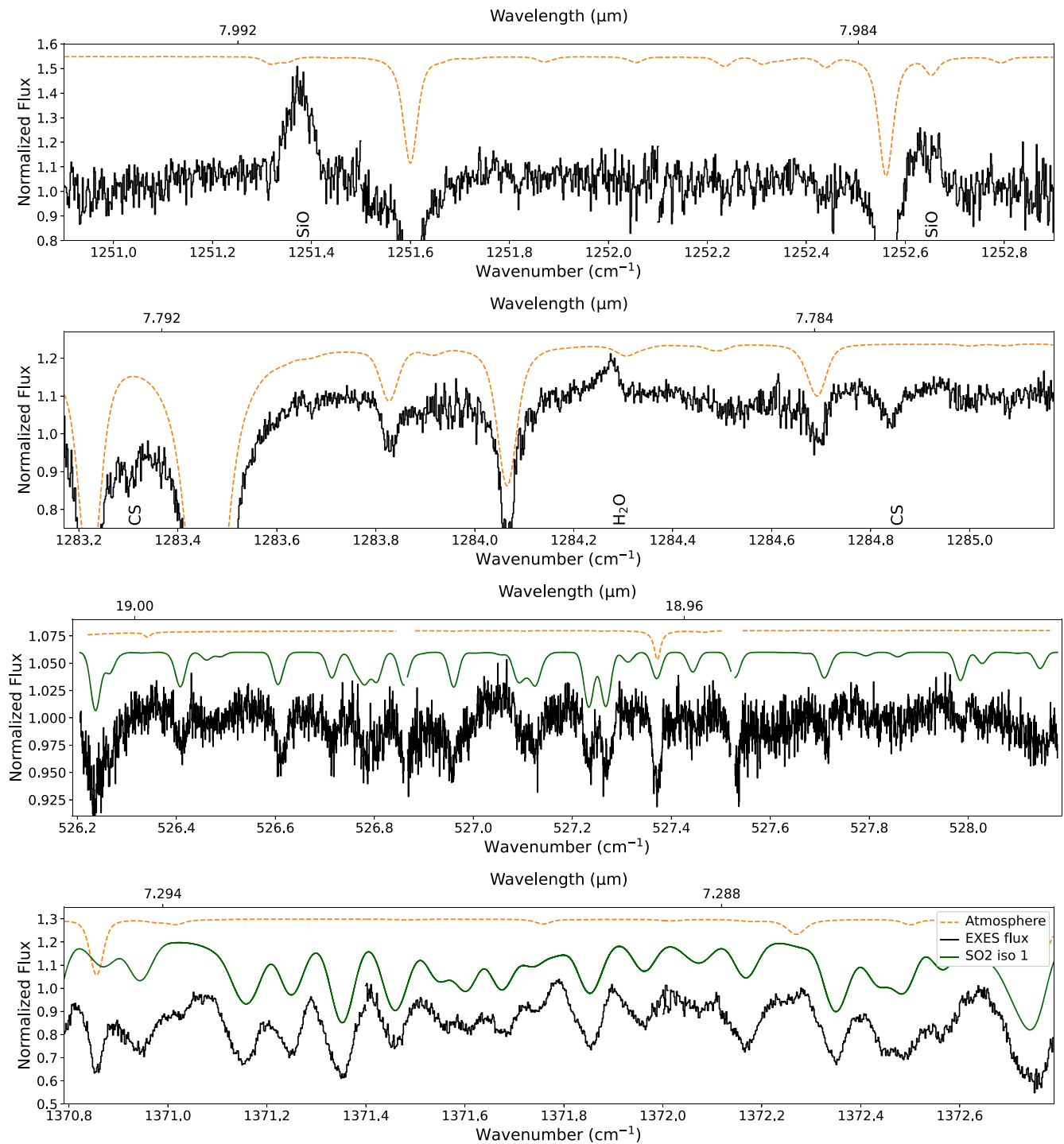
Figure 12. Examples of molecular transition lines observed with SOFIA/EXES (solid black) with offset atmospheric transmission (dotted orange). Species top to bottom: SiO; CS and H_2O; the ν_2 band of SO_2; and the ν_3 band of SO_2. The bottom two plots also include simulated spectra resulting from a fit to the data (solid green; Section 3.3).
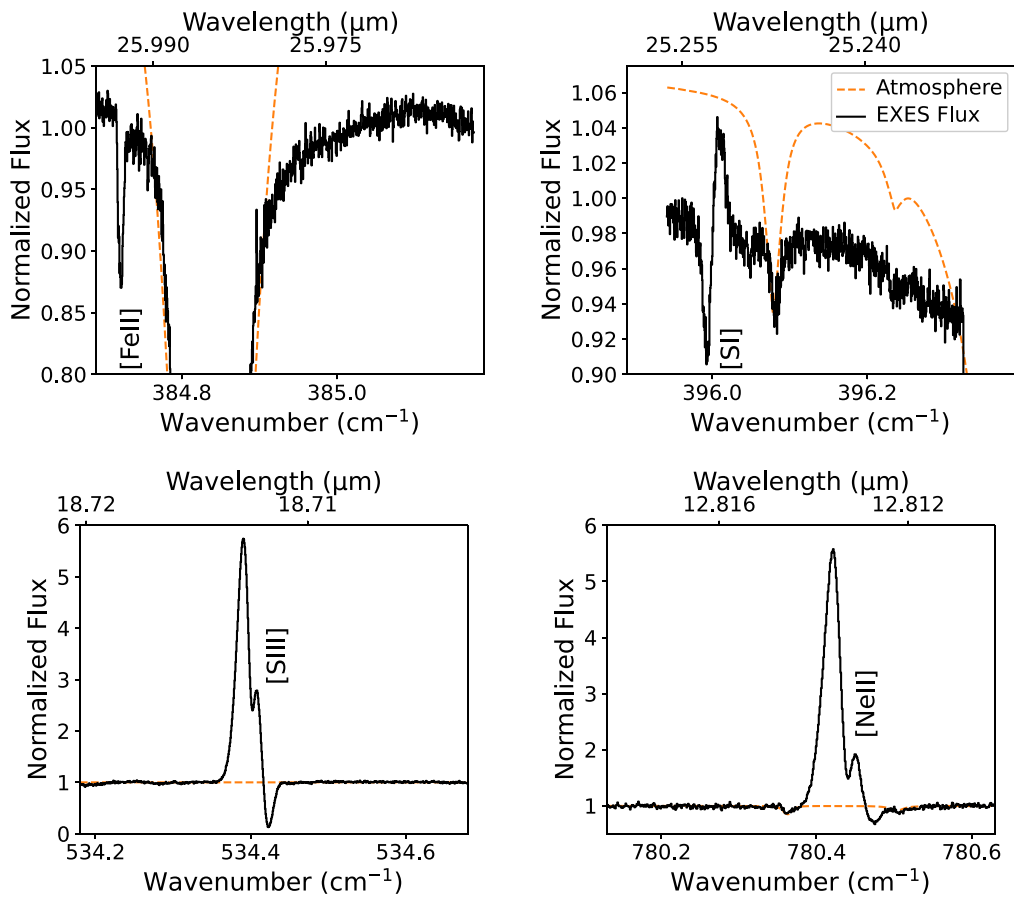
Figure 13. Examples of atomic forbidden transition lines observed with SOFIA/EXES (solid black) with offset atmospheric transmission (dotted orange). Transitions left to right, top to bottom: [Fe II], [S I], [S III], and [Ne II]. The emission lines are on-source toward IRc2, while the apparent absorption features are off-source emission lines that resulted from the nod subtraction. This creates a spurious P-cygni feature. In Section 3.4 we analyze the flux from the on- and off-source separately.

Appendix B
Gallery of EXES Beams

Figure 14 shows the EXES beam size and orientation for each setting in this work's survey overlayed on a 12.4 μm map of the region (Okumura et al. 2011).
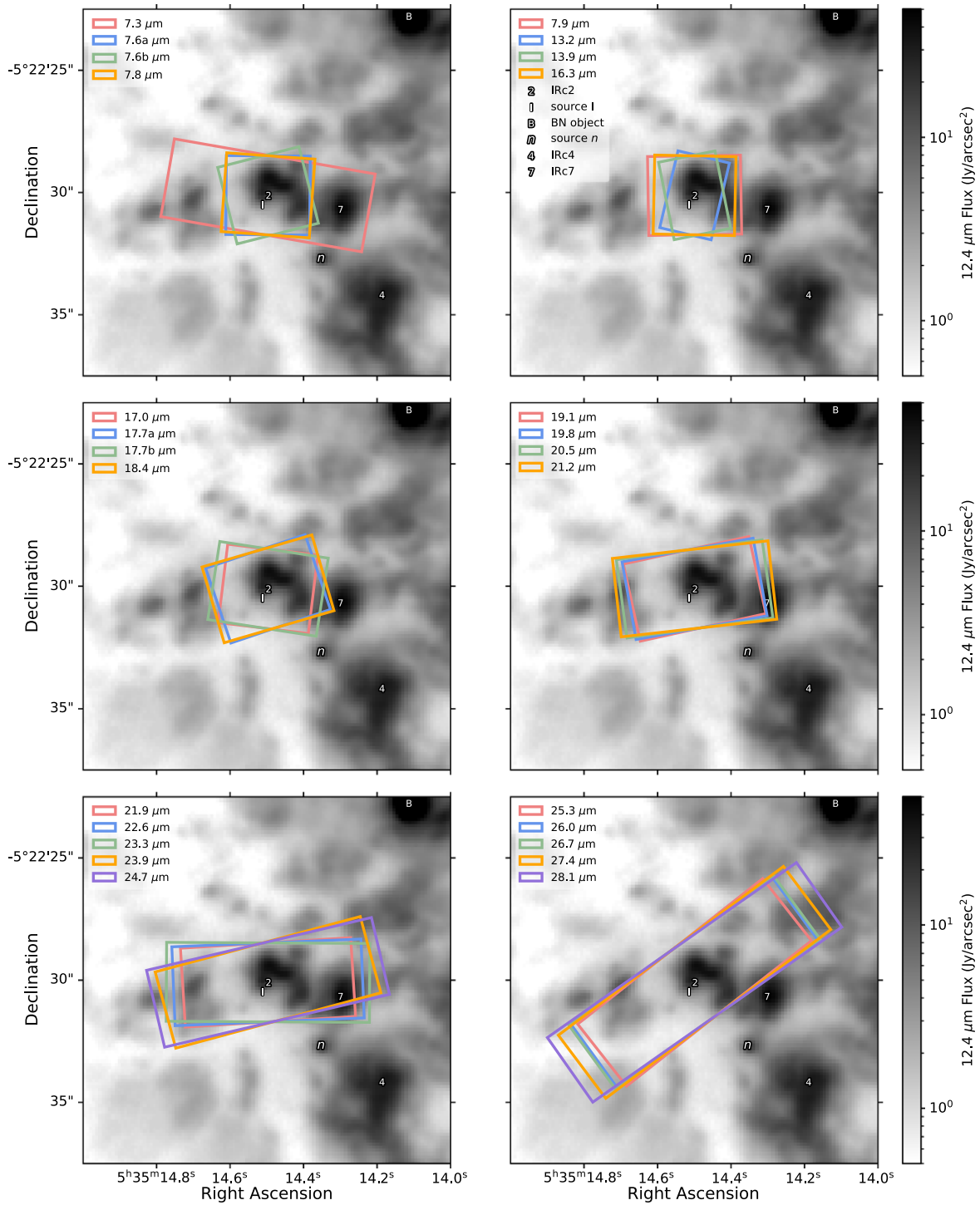
Figure 14. Colored boxes give the location, size, and orientation of the EXES beam for all settings in this work. The "2" for IRc2 is given at the beam's center for this survey. The grayscale background is the 12.4 μm map of the region from Okumura et al. (2011) taken with SUBARU/COMICS. Locations of other regional features are marked: source I, BN object, source n, IRc4, and IRc7. BN is located according to Gomez et al. (2005), while all other objects are located according to Okumura et al. (2011).

Appendix C
Comparison of Abundances

Table 10 gives the abundances estimated in this work's survey towards Orion IRc2 in the MIR, compared to abundances measured in the Orion hot core by selected longer wavelength surveys. Refer to Section 3.2 for a description of this work's abundance estimations.

Table 10
Abundances with Respect to Molecular Hydrogen Estimated in This Work Compared to the Orion Hot Core by Select Line Surveys at Longer Wavelengths

CS	HCN	HNC	NH$_3$	SO$_2$	Source
$(3.67 \pm 2.15) \times 10^{-8}$	$(3.85 \pm 2.25) \times 10^{-7}$	$(3.90 \pm 2.28) \times 10^{-9}$	$(8.32 \pm 6.29) \times 10^{-8}$	$(3.25 \pm 1.89) \times 10^{-7}$ (ν_2) $(5.79 \pm 3.36) \times 10^{-7}$ (ν_3)	This Work
1.40×10^{-7}	6.40×10^{-7}	8.70×10^{-10}	$\cdots$	6.20×10^{-7}	Crockett et al. (2014)
$\cdots$	$\cdots$	$\cdots$	$\cdots$	$(3.50 \pm 0.69) \times 10^{-7}$	Feng et al. (2016)
$\cdots$	$\cdots$	$\cdots$	$(4.0 \pm 2.1) \times 10^{-7}$ to $(6.0 \pm 3.5) \times 10^{-6}$	$4.70 \pm 0.80) \times 10^{-8}$	Gong et al. (2015)
$\cdots$	$\cdots$	$\cdots$	$\cdots$	$(2.90 \pm 1.50) \times 10^{-7}$	Luo et al. (2019)
2.90×10^{-9}	$\cdots$	4.40×10^{-11}	1.60×10^{-6}	$\cdots$	Persson et al. (2007)
6.00×10^{-9}	$\cdots$	$\cdots$	$\cdots$	1.20×10^{-7}	Sutton et al. (1995)
$5.00 \pm 1.19 \times 10^{-8}$	$\cdots$	$\cdots$	$\cdots$	$\cdots$	Tercero et al. (2010)

Note. Our abundances are totaled along the line of sight, i.e., the sum of the blue and red clumps for HCN (Table 3), while other species are blue clump only. For N_{H_2}, we use the column density of H$_2$ along the line of sight toward IRc2, $1.9 \pm 1.1 \times 10^{23}$ cm^{-2} (Evans et al. 1991). Abundances from Crockett et al. (2014) are those estimated by MADEX modeling except for CS, which is estimated by XCLASS modeling. NH$_3$ abundances as estimated by Gong et al. (2015) are given as a range over all transitions.

Appendix D
Observed Transitions

Tables 11 to 13 give the observed transitions and inferred parameters for lines observed in this survey. Tables 11 and 12 give the molecular absorption and emission lines respectively. Refer to Section 3.2 for how the inferred parameters were calculated. Table 13 gives atomic and ion lines and refer to Section 3.4 for how their inferred parameters were calculated.

Table 11
Observed Transitions and Inferred Parameters for Molecular Absorption Lines

Transition	Wavelength (μm)	Wavenumber (cm^{-1})	E_l/k_B (K)	g_l	A (s^{-1})	v_{LSR} (km s^{-1})	v_{FWHM} (km s^{-1})	τ_0 ($\times 10^{14}$ cm^{-2})	N_l
					ν_5 ortho-C_2H_2				
R21e	12.80816	780.75233	781.6	129	3.838	-8.9 ± 0.2	4.3 ± 0.6	0.111 ± 0.013	1.52 ± 0.22^b
R19e	12.88525	776.08101	643.0	117	3.761	-7.6 ± 0.4	8.2 ± 0.8	0.151 ± 0.009	3.94 ± 0.39^b
						1.9 ± 0.5	6.9 ± 1.1	0.094 ± 0.009	2.04 ± 0.36^r
R17e	12.96336	771.40482	517.8	105	3.689	-7.5 ± 0.2	7.8 ± 0.4	0.283 ± 0.010	6.94 ± 0.34^b
						2.1 ± 0.3	6.1 ± 0.6	0.136 ± 0.010	2.61 ± 0.28^r
R15e	13.04250	766.72409	406.2	93	3.622	-7.4 ± 0.2	8.9 ± 0.6	0.396 ± 0.015	11.01 ± 0.75^b
						2.0 ± 0.5	6.8 ± 1.1	0.145 ± 0.015	3.06 ± 0.60^r
R13e	13.12269	762.03916	308.0	81	3.562	-7.6 ± 0.2	7.3 ± 0.4	0.541 ± 0.021	12.20 ± 0.64^b
						0.7 ± 0.4	5.8 ± 0.9	0.182 ± 0.018	3.27 ± 0.56^r
R11e	13.20393	757.35035	223.4	69	3.509	-8.1 ± 0.7	8.8 ± 0.9	0.562 ± 0.123	15.16 ± 4.61^b
						$\cdots$	11.3 ± 2.8	0.278 ± 0.067	9.54 ± 4.46^b
R9e	13.28625	752.65799	152.3	57	3.467	-7.7 ± 0.4	9.3 ± 0.5	0.711 ± 0.049	19.59 ± 2.35^b
						0.7 ± 1.0	9.7 ± 1.2	0.317 ± 0.041	9.12 ± 2.18^r
R7e	13.36966	747.96239	94.8	45	3.438	-7.0 ± 0.3	10.1 ± 0.4	0.887 ± 0.022	25.69 ± 1.49^b
						1.4 ± 0.6	7.5 ± 0.7	0.290 ± 0.039	6.22 ± 1.30^r
R5e	13.45417	743.26389	50.8	33	3.433	-7.5 ± 0.4	8.9 ± 0.5	0.800 ± 0.039	19.36 ± 1.80^b
						1.3 ± 1.0	9.0 ± 1.3	0.304 ± 0.036	7.41 ± 1.78^r
R3e	13.53981	738.56281	20.3	21	3.48	-7.4 ± 0.3	7.0 ± 1.1	0.807 ± 0.100	$13.67 \pm 3.69^{b*}$
						-0.1 ± 1.4	10.3 ± 1.8	0.363 ± 0.056	$9.00 \pm 2.81^{r*}$
						$\cdots$	3.5 ± 1.0	0.224 ± 0.107	$1.91 \pm 1.38^{b*}$
R1e	13.62659	733.85945	3.4	9	3.693	-7.4 ± 0.1	8.6 ± 0.2	0.792 ± 0.013	11.72 ± 0.46^b
						0.6 ± 0.4	7.4 ± 0.7	0.197 ± 0.013	2.48 ± 0.37^r
Q21e	13.67576	731.22084	781.6	129	6.111	-7.2 ± 0.2	7.7 ± 0.4	0.143 ± 0.005	1.88 ± 0.11^b
						3.2 ± 0.5	8.6 ± 1.2	0.055 ± 0.004	0.80 ± 0.11^r
Q19e	13.68260	730.85539	643.0	117	6.102	-7.2 ± 0.2	7.5 ± 0.4	0.258 ± 0.008	3.32 ± 0.21^b
						1.3 ± 0.5	6.0 ± 1.2	0.068 ± 0.008	0.70 ± 0.15^r
Q17e	13.68878	730.52509	517.8	105	6.094	-7.9 ± 0.1	7.4 ± 0.2	0.420 ± 0.007	5.34 ± 0.15^b
						0.5 ± 0.2	6.1 ± 0.5	0.131 ± 0.007	1.36 ± 0.14^r
Q15e	13.69431	730.23009	406.2	93	6.086	-6.9 ± 0.1	7.5 ± 0.3	0.564 ± 0.012	$7.26 \pm 0.28^{b*}$
						$\cdots$	2.7 ± 0.5	0.149 ± 0.017	$0.70 \pm 0.14^{b*}$
Q13e	13.69918	729.97053	308.0	81	6.08	-7.0 ± 0.1	9.9 ± 0.5	0.740 ± 0.033	$12.51 \pm 1.16^{b*}$
						$\cdots$	2.6 ± 0.6	0.117 ± 0.015	$0.52 \pm 0.13^{b*}$
Q11e	13.70339	729.74654	223.4	69	6.072	-6.6 ± 0.1	10.4 ± 0.2	0.890 ± 0.012	$15.81 \pm 0.38^{b*}$
Q9e	13.70693	729.55822	152.3	57	6.07	-7.0 ± 0.1	9.4 ± 0.1	0.973 ± 0.009	15.67 ± 0.24^b
						2.4 ± 0.3	7.3 ± 0.4	0.180 ± 0.008	2.26 ± 0.20^r
Q7e	13.70979	729.40565	94.8	45	6.067	-7.1 ± 0.1	9.0 ± 0.2	0.991 ± 0.015	15.31 ± 0.49^b
						1.6 ± 0.5	8.8 ± 0.7	0.205 ± 0.014	3.09 ± 0.42^r
Q5e	13.71199	729.28892	50.8	33	6.063	-6.4 ± 0.1	8.0 ± 0.4	0.688 ± 0.030	$9.42 \pm 0.71^{b*}$
P3e	13.84863	722.09321	20.3	21	2.364	-7.3 ± 0.1	8.7 ± 0.2	0.633 ± 0.009	32.87 ± 1.10^b
						0.4 ± 0.3	6.4 ± 0.9	0.151 ± 0.012	5.74 ± 1.15^r
P5e	13.93953	717.3844	50.8	33	2.588	-7.1 ± 0.1	8.5 ± 0.2	0.719 ± 0.011	28.53 ± 0.86^b
						1.5 ± 0.4	7.7 ± 0.6	0.201 ± 0.011	7.26 ± 0.82^r
P7e	14.03165	712.67472	94.8	45	2.649	-7.0 ± 0.1	9.7 ± 0.2	0.757 ± 0.011	31.02 ± 0.49^b
P9e	14.12500	707.96448	152.3	57	2.663	-7.2 ± 0.1	9.4 ± 0.2	0.689 ± 0.011	25.77 ± 0.66^b
						2.5 ± 0.4	7.0 ± 0.8	0.136 ± 0.010	3.78 ± 0.54^r
					ν_5 para-C_2H_2				
R20e	12.84658	778.4173	710.6	41	3.799	-8.6 ± 0.4	5.8 ± 1.3	0.062 ± 0.010	1.13 ± 0.30^b
R16e	13.00280	769.065	460.3	33	3.654	-6.7 ± 0.3	9.8 ± 0.7	0.170 ± 0.008	5.26 ± 0.41^b
						3.6 ± 0.4	6.4 ± 0.8	0.100 ± 0.009	2.03 ± 0.30^r
R14e	13.08246	764.38213	355.4	29	3.591	-7.4 ± 0.2	8.3 ± 0.5	0.309 ± 0.011	8.02 ± 0.44^b
						2.2 ± 0.4	6.1 ± 0.8	0.121 ± 0.011	2.31 ± 0.34^r
R12e	13.16317	759.69522	264.0	25	3.535	-7.0 ± 0.2	8.4 ± 0.4	0.375 ± 0.012	9.65 ± 0.40^b
						2.3 ± 0.4	6.0 ± 0.8	0.135 ± 0.011	2.50 ± 0.34^r
R10e	13.24495	755.00459	186.2	21	3.486	-7.6 ± 0.2	7.8 ± 0.3	0.486 ± 0.014	11.36 ± 0.64^b

Table 11
(Continued)

Transition (μm)	Wavelength (cm^{-1})	Wavenumber (K)	E_l/k_B	g_l (s^{-1})	A (km s^{-1})	v_{LSR} (km s^{-1})	v_{FWHM}	τ_0 ($\times 10^{14}$ cm^{-2})	N_l
						1.3 ± 0.5	8.9 ± 0.9	0.191 ± 0.010	5.13 ± 0.66^{r}
R8e	13.32781	750.31057	121.9	17	3.45	-7.6 ± 0.2	13.2 ± 0.6	0.556 ± 0.014	$21.56 \pm 0.79^{b*}$
						3.7 ± 0.4	6.0 ± 1.0	0.128 ± 0.018	$2.26 \pm 0.55^{r*}$
R6e	13.41177	745.61349	71.1	13	3.432	-7.2 ± 0.1	8.9 ± 0.3	0.677 ± 0.017	16.84 ± 0.56^{b}
						3.0 ± 0.4	7.3 ± 0.7	0.218 ± 0.014	4.43 ± 0.49^{r}
R4e	13.49685	740.91365	33.9	9	3.447	-6.8 ± 0.2	10.6 ± 0.6	0.719 ± 0.028	$19.77 \pm 1.12^{b*}$
						$\cdots$	2.2 ± 0.4	0.417 ± 0.059	$2.39 \pm 0.46^{b*}$
Q24e	13.66429	731.83453	1014.9	49	6.127	-8.1 ± 0.2	5.2 ± 0.7	0.046 ± 0.005	0.41 ± 0.07^{b}
R0e	13.67041	731.50702	0.0	1	4.07	-7.2 ± 0.2	8.2 ± 0.5	0.488 ± 0.015	3.42 ± 0.23^{b}
						0.7 ± 0.5	5.5 ± 1.0	0.120 ± 0.015	0.56 ± 0.13^{r}
Q20e	13.67926	731.03373	710.6	41	6.108	-8.0 ± 0.2	5.3 ± 0.5	0.094 ± 0.007	0.85 ± 0.10^{b}
Q18e	13.68577	730.68584	578.7	37	6.099	-7.8 ± 0.1	7.8 ± 0.3	0.158 ± 0.004	2.10 ± 0.09^{b}
						0.9 ± 0.4	6.1 ± 0.8	0.049 ± 0.004	0.51 ± 0.08^{r}
Q16e	13.69163	730.37317	460.3	33	6.091	-7.2 ± 0.1	7.3 ± 0.3	0.292 ± 0.007	3.66 ± 0.18^{b}
						1.2 ± 0.4	6.6 ± 0.9	0.081 ± 0.006	0.92 ± 0.14^{r}
Q12e	13.70137	729.85409	264.0	25	6.077	-7.6 ± 0.2	8.1 ± 0.3	0.594 ± 0.028	$8.19 \pm 0.63^{b*}$
						$\cdots$	10.0 ± 1.3	0.221 ± 0.013	$3.79 \pm 0.65^{b*}$
Q8e	13.70844	729.47746	121.9	17	6.067	-8.4 ± 0.2	6.5 ± 1.0	0.466 ± 0.176	$5.22 \pm 2.74^{b*}$
						$\cdots$	12.1 ± 3.7	0.323 ± 0.083	$6.70 \pm 3.75^{b*}$
Q6e	13.71097	729.3428	71.1	13	6.065	-7.5 ± 0.1	8.2 ± 0.3	0.694 ± 0.018	$9.72 \pm 0.53^{b*}$
						1.8 ± 0.6	9.6 ± 1.7	0.153 ± 0.007	$2.51 \pm 0.46^{r*}$
Q4e	13.71283	729.244	33.9	9	6.061	-6.7 ± 0.1	7.7 ± 0.5	0.500 ± 0.030	$6.59 \pm 0.82^{b*}$
P2e	13.80363	724.4472	10.2	5	1.986	-7.5 ± 0.1	8.1 ± 0.2	0.328 ± 0.006	22.80 ± 0.62^{b}
						1.5 ± 0.3	6.2 ± 0.6	0.091 ± 0.005	4.85 ± 0.51^{r}
P8e	14.07817	710.31965	121.9	17	2.659	-6.8 ± 0.1	9.3 ± 0.3	0.472 ± 0.011	17.84 ± 0.63^{b}
P10e	14.17215	705.60925	186.2	21	2.663	-8.0 ± 0.4	8.0 ± 0.5	0.342 ± 0.025	10.74 ± 1.37^{b}
						-0.1 ± 1.4	8.9 ± 2.0	0.108 ± 0.019	3.75 ± 1.39^{r}
				ν_5 ^{13}CCH$_2$					
R10e	13.27221	753.45375	181.7	168	3.071	-8.2 ± 0.4	7.0 ± 1.0	0.072 ± 0.008	1.73 ± 0.27^{b}
R9e	13.31267	751.16424	148.7	152	3.056	-6.6 ± 0.3	5.6 ± 1.0	0.071 ± 0.009	1.34 ± 0.30^{b}
R7e	13.39436	746.58267	92.5	120	3.033	-7.7 ± 0.3	7.5 ± 0.8	0.099 ± 0.009	2.40 ± 0.25^{b}
						2.0 ± 0.5	3.9 ± 1.1	0.049 ± 0.011	0.62 ± 0.16^{r}
R6e	13.43561	744.29068	69.4	104	3.026	-6.0 ± 0.5	10.2 ± 1.7	0.091 ± 0.011	2.95 ± 0.62^{b}
R5e	13.47713	741.99794	49.6	88	3.027	-7.9 ± 0.2	7.0 ± 0.4	0.128 ± 0.006	$2.75 \pm 0.21^{b*}$
						4.6 ± 3.3	10.6 ± 5.8	0.035 ± 0.008	$1.15 \pm 0.82^{r*}$
						$\cdots$	4.5 ± 2.6	0.027 ± 0.029	$0.37 \pm 0.59^{b*}$
R4e	13.51891	739.7045	33.0	72	3.038	-7.5 ± 0.2	7.5 ± 0.4	0.143 ± 0.005	3.11 ± 0.18^{b}
						2.1 ± 0.7	8.1 ± 1.6	0.038 ± 0.004	0.91 ± 0.22^{r}
R3e	13.56097	737.41038	19.8	56	3.066	-7.7 ± 0.3	6.8 ± 0.5	0.119 ± 0.014	2.22 ± 0.40^{b}
						-0.2 ± 2.0	10.0 ± 3.3	0.035 ± 0.006	0.95 ± 0.44^{r}
R2e	13.60330	735.11563	9.9	40	3.123	-7.4 ± 0.1	6.5 ± 0.4	0.122 ± 0.006	1.93 ± 0.17^{b}
						$\cdots$	3.8 ± 0.9	0.033 ± 0.006	0.30 ± 0.09^{b}
R1e	13.64591	732.82028	3.3	24	3.249	-7.4 ± 0.2	4.5 ± 0.8	0.072 ± 0.014	$0.63 \pm 0.21^{b*}$
						$\cdots$	12.9 ± 3.5	0.044 ± 0.005	$1.11 \pm 0.40^{b*}$
						$\cdots$	2.4 ± 0.7	0.031 ± 0.007	$0.14 \pm 0.05^{b*}$
P5e	13.95207	716.73929	49.6	88	2.253	-7.3 ± 0.2	5.7 ± 0.6	0.076 ± 0.006	2.34 ± 0.26^{b}
				$\nu_4 + \nu_5$ ortho-C$_2$H$_2$					
P1e	7.54307	1325.720103	3.4	9	4.324	-8.7 ± 0.4	7.7 ± 0.6	0.265 ± 0.017	88.86 ± 10.26^{b}
						0.5 ± 0.6	9.7 ± 1.1	0.185 ± 0.011	77.65 ± 10.87^{r}
P3e	7.56981	1321.036604	20.3	21	2.578	-7.7 ± 0.4	9.4 ± 0.7	0.532 ± 0.021	168.32 ± 14.55^{b}
						2.1 ± 0.6	8.6 ± 1.0	0.277 ± 0.021	79.91 ± 12.92^{r}
P5e	7.59657	1316.383626	50.8	33	2.371	-7.2 ± 0.4	12.0 ± 0.7	0.568 ± 0.018	214.35 ± 13.50^{b}
						2.0 ± 0.5	5.7 ± 1.1	0.182 ± 0.037	32.43 ± 7.17^{r}
P7e	7.62334	1311.760274	94.8	45	2.282	-7.9 ± 0.2	6.6 ± 0.3	0.551 ± 0.018	111.34 ± 6.65^{b}
						0.0 ± 0.3	8.0 ± 0.6	0.339 ± 0.012	82.81 ± 7.04^{r}
P9e	7.65014	1307.16496	152.3	57	2.228	-7.6 ± 0.3	7.7 ± 0.5	0.454 ± 0.031	105.10 ± 12.31^{b}
						1.3 ± 0.7	10.0 ± 1.2	0.279 ± 0.017	83.72 ± 12.66^{r}
P11e	7.67698	1302.595406	223.4	69	2.188	-6.8 ± 0.2	6.1 ± 0.4	0.356 ± 0.017	64.63 ± 5.38^{b}
						1.2 ± 0.5	7.3 ± 1.0	0.185 ± 0.013	39.98 ± 5.88^{r}
P13e	7.70387	1298.048655	308.0	81	2.155	-7.5 ± 0.2	7.7 ± 0.6	0.217 ± 0.012	$49.19 \pm 3.56^{b*}$
						0.9 ± 0.3	4.8 ± 0.6	0.152 ± 0.014	$21.25 \pm 2.69^{r*}$
P15e	7.73084	1293.521104	406.2	93	2.124	-6.6 ± 0.2	7.9 ± 0.6	0.160 ± 0.008	36.58 ± 2.97^{b}
						2.5 ± 0.3	5.8 ± 0.8	0.086 ± 0.008	14.61 ± 2.24^{r}

Table 11
(Continued)

Transition	Wavelength (μm)	Wavenumber (cm^{-1})	E_l/k_B (K)	g_l	A (s^{-1})	v_{LSR} (km s^{-1})	v_{FWHM} (km s^{-1})	τ_0	N_l ($\times10^{14}$cm^{-2})
					$\nu_4 + \nu_5$ para-C$_2$H$_2$				
R0e	7.51634	1330.434328	0.0	1	1.451	-8.5 ± 0.4	12.4 ± 1.4	0.146 ± 0.011	26.27 ± 3.64[b]
						2.3 ± 0.4	4.5 ± 1.0	0.087 ± 0.015	5.68 ± 1.42[r]
P2e	7.55644	1323.374509	10.2	5	2.874	-7.6 ± 0.2	8.8 ± 0.6	0.238 ± 0.012	74.79 ± 4.75[b]
						1.3 ± 0.2	4.4 ± 0.5	0.161 ± 0.015	25.34 ± 3.17[r]
P4e	7.58319	1318.706339	33.9	9	2.447	-7.6 ± 0.2	6.3 ± 0.4	0.280 ± 0.014	56.91 ± 4.88[b]
						1.2 ± 0.5	9.5 ± 1.1	0.163 ± 0.010	49.80 ± 6.91[r]
P6e	7.60995	1314.06833	71.1	13	2.32	-8.3 ± 0.6	7.1 ± 1.4	0.253 ± 0.033	55.84 ± 15.92[b]
						0.2 ± 1.4	9.9 ± 2.5	0.169 ± 0.022	51.58 ± 17.84[r]
P8e	7.63674	1309.459238	121.9	17	2.253	-7.3 ± 0.2	6.4 ± 0.3	0.274 ± 0.009	53.05 ± 2.92[b]
						1.5 ± 0.3	8.2 ± 0.6	0.170 ± 0.007	42.04 ± 3.34[r]
					ν_4 CH$_4$				
R4(E)	7.50511	1332.424711	150.7	18	2.327	-7.9 ± 0.3	7.8 ± 0.6	0.381 ± 0.020	65.79 ± 5.60[b]
						1.6 ± 0.4	7.2 ± 1.0	0.219 ± 0.018	35.27 ± 5.22[r]
R4(F2)	7.50703	1332.085188	150.8	27	2.326	-7.7 ± 0.2	7.7 ± 0.4	0.442 ± 0.016	75.71 ± 4.15[b]
						1.0 ± 0.3	6.1 ± 0.5	0.282 ± 0.016	38.25 ± 3.59[r]
R3(A2)	7.53537	1327.07402	90.5	35	2.322	-7.1 ± 0.3	8.9 ± 1.3	0.574 ± 0.021	107.08 ± 14.29[b]
						1.4 ± 0.6	6.7 ± 0.8	0.321 ± 0.044	45.03 ± 10.80[r]
R2(F2)	7.56381	1322.085048	45.2	15	2.317	-8.6 ± 0.2	6.9 ± 0.8	0.572 ± 0.031	75.72 ± 11.60[b*]
						-0.6 ± 0.7	9.9 ± 1.0	0.298 ± 0.019	56.12 ± 8.91[r*]
R1(F1)	7.59401	1316.82689	15.1	9	2.309	-8.2 ± 0.2	6.8 ± 0.4	0.518 ± 0.023	55.67 ± 4.47[b]
						0.0 ± 0.5	8.1 ± 0.9	0.289 ± 0.016	37.00 ± 4.67[r]
Q4(F1)	7.66735	1304.23207	150.7	27	2.259	-8.1 ± 0.4	7.2 ± 0.6	0.372 ± 0.028	70.52 ± 9.17[b]
						0.3 ± 0.8	9.5 ± 1.5	0.202 ± 0.015	50.64 ± 9.86[r]
					ν CS				
R11	7.74690	1290.839259	155.1	23	8.11	-4.2 ± 0.7	13.0 ± 3.2	0.049 ± 0.009	4.18 ± 1.57[b]
R10	7.75585	1289.349312	129.3	21	8.04	-7.3 ± 0.3	7.8 ± 0.8	0.083 ± 0.007	4.23 ± 0.46[b]
R8	7.77404	1286.332863	84.6	17	7.88	-4.1 ± 0.5	12.1 ± 1.4	0.070 ± 0.007	5.48 ± 0.66[b]
R7	7.78327	1284.806427	65.8	15	7.79	-6.3 ± 0.3	9.9 ± 0.7	0.083 ± 0.005	5.28 ± 0.40[b]
R6	7.79261	1283.267891	49.4	13	7.68	-6.9 ± 0.3	5.7 ± 0.9	0.109 ± 0.012	3.96 ± 0.66[b]
R5	7.80203	1281.717289	35.3	11	7.56	-7.3 ± 0.4	7.2 ± 1.0	0.075 ± 0.009	3.41 ± 0.50[b]
R4	7.81156	1280.154654	23.5	9	7.4	-5.7 ± 0.4	8.1 ± 1.3	0.065 ± 0.008	3.26 ± 0.60[b]
R3	7.82118	1278.580017	14.1	7	7.2	-7.7 ± 0.5	7.1 ± 1.3	0.079 ± 0.012	3.36 ± 0.66[b]
R2	7.83089	1276.99341	7.1	5	6.91	-8.1 ± 0.3	6.5 ± 0.8	0.059 ± 0.005	2.20 ± 0.29[b]
					Pure Rotational H$_2$O				
$5_{4,1}-4_{1,4}$	25.94015	385.502803	323.5	27	0.0264	-8.0 ± 0.4	17.0 ± 1.0	0.423 ± 0.013	341.22 ± 30.58[b*]
					ν_2 HCN				
R15e	13.17206	759.182446	510.2	186	1.278	-7.3 ± 0.6	7.6 ± 1.0	0.143 ± 0.011	9.31 ± 1.58[b]
						1.3 ± 0.8	8.4 ± 1.4	0.108 ± 0.009	7.76 ± 1.62[r]
R13e	13.27497	753.297564	386.9	162	1.254	-7.9 ± 0.3	6.0 ± 0.7	0.247 ± 0.046	12.54 ± 3.54[b]
						-0.5 ± 1.6	12.0 ± 3.0	0.139 ± 0.015	14.14 ± 4.73[r]
R12e	13.32706	750.352972	331.7	150	1.242	-7.5 ± 0.1	7.9 ± 0.3	0.420 ± 0.015	28.00 ± 1.26[b*]
R11e	13.37959	747.407049	280.7	138	1.231	-7.3 ± 0.3	9.9 ± 0.5	0.468 ± 0.013	38.86 ± 2.47[b]
						1.4 ± 0.7	7.9 ± 1.1	0.138 ± 0.021	9.12 ± 2.33[r]
R10e	13.43256	744.459871	233.9	126	1.221	-7.9 ± 0.2	8.1 ± 0.4	0.574 ± 0.017	38.59 ± 2.37[b]
						0.5 ± 0.6	7.9 ± 0.9	0.208 ± 0.017	13.56 ± 2.32[r]
R7e	13.59413	735.611573	119.1	90	1.194	-7.5 ± 0.2	8.3 ± 0.2	0.760 ± 0.018	49.65 ± 2.16[b]
						0.9 ± 0.7	8.9 ± 0.9	0.183 ± 0.014	12.83 ± 2.13[r]
R6e	13.64889	732.660136	89.3	78	1.187	-7.2 ± 0.2	6.7 ± 0.8	0.698 ± 0.091	35.76 ± 8.44[b*]
						-1.0 ± 1.4	11.0 ± 1.6	0.272 ± 0.042	22.99 ± 6.66[r*]
						$\cdots$	3.5 ± 0.7	0.183 ± 0.073	4.97 ± 2.84[b*]
R5e	13.70412	729.70782	63.8	66	1.183	-7.3 ± 0.1	11.6 ± 0.2	0.755 ± 0.013	65.02 ± 1.25[b*]
R4e	13.75980	726.7547	42.5	54	1.184	-7.3 ± 0.1	8.7 ± 0.2	0.780 ± 0.013	47.97 ± 1.81[b]
						1.1 ± 0.6	7.5 ± 1.1	0.154 ± 0.014	8.20 ± 1.69[r]
R3e	13.81596	723.800848	25.5	42	1.19	-7.2 ± 0.1	9.4 ± 0.3	0.779 ± 0.019	48.37 ± 2.25[b]
						2.1 ± 0.3	7.6 ± 0.7	0.212 ± 0.018	10.63 ± 1.85[r]
R1e	13.92969	717.89124	4.3	18	1.251	-7.2 ± 0.1	8.5 ± 0.1	0.700 ± 0.007	28.23 ± 0.54[b]
						1.4 ± 0.2	6.5 ± 0.4	0.152 ± 0.007	4.66 ± 0.40[r]
R0e	13.98727	714.935627	0.0	6	1.371	-6.7 ± 0.3	9.7 ± 0.5	0.438 ± 0.011	10.12 ± 0.63[b*]
						2.4 ± 0.8	8.0 ± 1.4	0.112 ± 0.014	2.13 ± 0.57[r*]
Q14e	14.01526	713.5078	446.5	174	2.026	-7.8 ± 0.2	6.1 ± 0.3	0.309 ± 0.010	9.08 ± 0.65[b*]

Table 11
(Continued)

Transition	Wavelength (cm^{-1})	Wavenumber (K)	E_l/k_B	g_l	A (s^{-1})	v_{LSR} (km s^{-1})	v_{FWHM} (km s^{-1})	τ_0 ($\times 10^{14}$ cm^{-2})	N_l
						0.2 ± 0.7	8.0 ± 1.2	0.109 ± 0.007	4.18 ± 0.81[r*]
						$\cdots$	3.2 ± 0.8	0.086 ± 0.032	1.33 ± 0.79[r*]
Q13e	14.01926	713.304602	386.9	162	2.026	-7.3 ± 0.2	7.2 ± 0.3	0.419 ± 0.015	14.52 ± 0.99[b]
						-0.1 ± 0.7	7.6 ± 1.0	0.134 ± 0.013	4.87 ± 1.00[r]
Q11e	14.02640	712.941315	280.7	138	2.027	-7.4 ± 0.1	8.1 ± 0.3	0.592 ± 0.011	23.04 ± 0.75[b*]
						2.7 ± 0.7	5.9 ± 1.8	0.140 ± 0.011	3.96 ± 1.23[r*]
						$\cdots$	3.2 ± 1.0	0.117 ± 0.049	1.78 ± 1.21[r*]
Q10e	14.02955	712.781294	233.9	126	2.027	-7.0 ± 0.1	8.5 ± 0.2	0.673 ± 0.007	27.23 ± 0.53[b]
						$\cdots$	4.6 ± 0.6	0.117 ± 0.009	2.58 ± 0.37[b]
Q9e	14.03241	712.635726	191.4	114	2.028	-7.4 ± 0.1	12.4 ± 0.2	0.692 ± 0.010	41.06 ± 0.68[b]
Q8e	14.03500	712.504639	153.1	102	2.028	-7.0 ± 0.3	8.3 ± 0.3	0.772 ± 0.018	30.55 ± 1.60[b*]
						1.1 ± 0.5	7.7 ± 0.8	0.189 ± 0.017	6.97 ± 1.22[r*]
						$\cdots$	3.8 ± 1.1	0.097 ± 0.041	1.76 ± 1.18[b*]
Q7e	14.03729	712.388056	119.1	90	2.028	-6.9 ± 0.1	8.9 ± 0.2	0.801 ± 0.011	34.08 ± 0.71[b]
						$\cdots$	3.4 ± 0.8	0.081 ± 0.017	1.29 ± 0.43[b]
Q6e	14.03930	712.286	89.3	78	2.028	-7.0 ± 0.1	9.7 ± 0.3	0.750 ± 0.017	34.76 ± 1.11[b]
						$\cdots$	4.4 ± 0.6	0.180 ± 0.019	3.75 ± 0.63[b]
P2e	14.16297	706.0664	12.8	30	0.6576	-7.5 ± 0.2	7.8 ± 0.3	0.352 ± 0.008	65.46 ± 3.32[b]
						0.7 ± 0.3	7.5 ± 0.6	0.173 ± 0.009	30.99 ± 3.46[r]
P3e	14.22254	703.109429	25.5	42	0.778	-6.8 ± 0.3	11.1 ± 1.0	0.429 ± 0.029	79.92 ± 8.57[b*]
					ν_2 H^{13}CN				
R8e	13.66420	731.839651	149.2	204	1.157	-5.7 ± 0.3	7.0 ± 0.8	0.054 ± 0.005	3.05 ± 0.40[b]
R6e	13.77224	726.098321	87.0	156	1.143	-6.5 ± 0.2	8.2 ± 0.6	0.083 ± 0.005	5.30 ± 0.44[b]
R1e	14.05041	711.72312	4.1	36	1.206	-7.5 ± 0.4	8.7 ± 0.9	0.059 ± 0.005	2.46 ± 0.27[b]
					$2\nu_2$ HCN				
P10e	7.23320	1382.513753	233.9	126	1.117	-6.3 ± 0.3	9.6 ± 0.6	0.192 ± 0.006	129.23 ± 9.42[b]
						2.4 ± 0.6	6.8 ± 1.1	0.072 ± 0.010	33.96 ± 8.18[r]
P12e	7.26273	1376.892237	331.7	150	1.1	-5.3 ± 1.1	7.8 ± 1.9	0.108 ± 0.015	58.49 ± 19.94[b]
						1.2 ± 1.8	6.1 ± 2.5	0.050 ± 0.025	21.17 ± 17.72[r]
					ν_2 HNC				
R10e	20.16417	495.92916	239.3	126	2.197	-5.9 ± 0.5	8.4 ± 1.3	0.026 ± 0.004	0.30 ± 0.07[b]
R9e	20.28742	492.91629	195.8	114	2.163	-7.8 ± 0.3	12.9 ± 0.9	0.043 ± 0.002	0.75 ± 0.06[b]
R8e	20.41225	489.902	156.6	102	2.131	-6.2 ± 0.3	9.2 ± 1.0	0.042 ± 0.003	0.51 ± 0.08[b]
R7e	20.53867	486.88636	121.8	90	2.102	-7.7 ± 0.3	12.4 ± 1.0	0.048 ± 0.003	0.78 ± 0.07[b]
R5e	20.79645	480.85136	65.3	66	2.055	-8.2 ± 0.2	9.3 ± 0.5	0.071 ± 0.003	0.81 ± 0.04[b]
R3e	21.06097	474.8119	26.1	42	2.037	-8.0 ± 0.2	11.3 ± 0.6	0.081 ± 0.003	1.01 ± 0.08[b]
R2e	21.19584	471.7907	13.1	30	2.053	-8.1 ± 0.2	12.3 ± 0.8	0.076 ± 0.003	0.92 ± 0.08[b]
R1e	21.33249	468.76863	4.4	18	2.113	-8.0 ± 0.2	14.6 ± 0.7	0.069 ± 0.003	0.79 ± 0.05[b]
R0e	21.47094	465.74576	0.0	6	2.298	-8.3 ± 0.3	11.9 ± 1.3	0.037 ± 0.003	0.17 ± 0.03[b]
Q12e	21.53525	464.35494	339.3	150	3.404	-5.9 ± 0.6	8.6 ± 1.6	0.013 ± 0.002	0.09 ± 0.02[b]
Q11e	21.54687	464.10446	287.1	138	3.4	-8.1 ± 0.5	7.7 ± 2.5	0.022 ± 0.005	0.13 ± 0.07[b]
Q9e	21.56727	463.66551	195.8	114	3.393	-7.7 ± 0.3	10.5 ± 1.0	0.037 ± 0.002	0.30 ± 0.04[b]
Q8e	21.57604	463.47714	156.6	102	3.39	-7.7 ± 0.3	12.6 ± 1.0	0.055 ± 0.003	0.54 ± 0.06[b]
Q6e	21.59068	463.16287	91.4	78	3.385	-8.4 ± 0.2	13.2 ± 0.5	0.078 ± 0.003	0.81 ± 0.04[b]
Q5e	21.59654	463.03705	65.3	66	3.383	-8.3 ± 0.1	10.7 ± 0.4	0.082 ± 0.002	0.69 ± 0.04[b]
Q4e	21.60144	462.93214	43.5	54	3.382	-8.4 ± 0.2	11.6 ± 0.6	0.080 ± 0.003	0.72 ± 0.05[b]
Q3e	21.60536	462.84818	26.1	42	3.38	-8.9 ± 0.1	11.7 ± 0.6	0.080 ± 0.003	0.73 ± 0.06[b]
Q2e	21.60830	462.78519	13.1	30	3.379	-8.1 ± 0.2	12.8 ± 1.2	0.071 ± 0.004	0.71 ± 0.10[b]
Q1e	21.61026	462.74319	4.4	18	3.379	-8.9 ± 0.2	10.3 ± 0.7	0.057 ± 0.003	0.46 ± 0.04[b]
P3e	22.04352	453.64798	26.1	42	1.269	-6.8 ± 0.3	12.6 ± 1.5	0.031 ± 0.003	1.09 ± 0.20[b]
P5e	22.34156	447.5964	65.3	66	1.352	-7.0 ± 0.2	10.6 ± 0.5	0.041 ± 0.001	0.94 ± 0.05[b]
P6e	22.49363	444.57022	91.4	78	1.353	-5.3 ± 0.4	14.4 ± 2.0	0.029 ± 0.003	0.86 ± 0.19[b]
P7e	22.64781	441.54388	121.8	90	1.345	-9.1 ± 0.3	10.5 ± 1.3	0.031 ± 0.003	0.65 ± 0.11[b]
P8e	22.80411	438.51747	156.6	102	1.33	-7.9 ± 0.3	11.8 ± 1.1	0.028 ± 0.002	0.64 ± 0.08[b]
					ν_2 NH$_3$				
^{Q}P(4,0)a	11.71210	853.817812	285.6	108	6.559	-6.4 ± 0.3	5.2 ± 0.7	0.222 ± 0.026	3.79 ± 0.44[b]
^{Q}P(4,1)a	11.71580	853.548188	280.3	54	6.255	-6.7 ± 0.5	4.7 ± 1.1	0.145 ± 0.031	2.32 ± 0.50[b*]
^{Q}P(4,2)a	11.72711	852.72474	264.4	54	5.009	-5.3 ± 1.1	8.6 ± 4.8	0.153 ± 0.063	5.59 ± 4.50[b]

Table 11
(Continued)

Transition	Wavelength (μm)	Wavenumber (cm^{-1})	E_l/k_B (K)	g_l (s^{-1})	A (km s^{-1})	$v_{\rm LSR}$ (km s^{-1})	$v_{\rm FWHM}$	τ_0 ($\times 10^{14}$cm^{-2})	N_l
^{Q}P(4,3)a	11.74637	851.326935	237.8	108	2.928	-6.2 ± 0.4	4.7 ± 1.2	0.201 ± 0.041	6.84 ± 1.85^b
^{Q}P(6,3)s	11.79832	847.578094	550.4	156	4.36	-8.9 ± 1.3	10.3 ± 3.8	0.049 ± 0.014	2.24 ± 0.95^b

Note. Wavelength and wavenumber are the rest value for each transition, E_l is the energy level of the lower state, k_B is the Boltzmann constant, g_l is the lower statistical weight, A is the Einstein coefficient, $v_{\rm LSR}$ is the observed local standard of rest velocity at the transition's center, $v_{\rm FWHM}$ is the observed FWHM, τ_0 is the observed optical depth, and N_l is the observed column density of the transition as calculated in Equation (4). Data in the first six columns are from the HITRAN database (Gordon et al. 2017) for most species, and the GEISA database for HNC (Jacquinet-Husson et al. 2016). Superscript letters in the final column refer to which velocity component N_l will be totaled toward for the rotation diagrams: ^{b}blue clump, ^{r}red clump. The velocity for lines with more than one Gaussian is taken to be the that of the line with the largest τ_0, and the other Gaussian is recorded without velocity and in italics. Lines marked with * are blended with either the atmosphere (the majority of cases) or other transitions toward IRc2, and may be compromised to some degree.

(This table is available in machine-readable form.)

Table 12
Observed Transitions and Inferred Parameters for Molecular Emission Lines

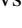| Transition	Wavelength (μm)	Wavenumber (cm^{-1})	E_u/k_B (K)	g_u	A (s^{-1})	$v_{\rm LSR}$ (km s^{-1})	$v_{\rm FWHM}$ (km s^{-1})	$S_{\rm Ja} \times S_{\nu 0}$ (Jy arcsec^{-2})	N_u
					Pure Rotational H$_2$				($\times 10^{19}$cm^{-2})
S(1)	17.03485	587.032	1015.1	21	4.758×10^{-10}	-10.7 ± 2.6	19.2 ± 5.1	0.740 ± 0.089	8.55 ± 2.49^b
						0.5 ± 0.5	9.3 ± 1.8	0.795 ± 0.258	4.45 ± 1.68^r
					ν_2 H$_2$O				($\times 10^9$cm^{-2})
$8_{3,5}-9_{4,6}$	7.51934	1329.90473	3842.7	17	4.377	8.9 ± 0.3	11.1 ± 1.0	0.791 ± 0.053	5.77 ± 0.63
$9_{3,6}-10_{4,7}$	7.55667	1323.33442	4179.2	57	3.903	9.9 ± 0.4	12.5 ± 1.2	0.900 ± 0.066	8.24 ± 0.99
$5_{1,5}-6_{2,4}$	7.57544	1320.05555	2766.5	11	0.6821	8.1 ± 0.1	9.3 ± 0.3	3.381 ± 0.096	131.77 ± 5.98
$6_{2,5}-7_{3,4}$	7.58191	1318.92943	3109.6	39	2.174	7.2 ± 0.1	10.7 ± 0.2	10.005 ± 0.171	141.65 ± 3.99
$7_{4,3}-8_{5,4}$	7.59317	1316.9724	3700.7	45	7.502	8.1 ± 0.1	9.4 ± 0.3	3.315 ± 0.081	11.88 ± 0.48
$7_{4,4}-8_{5,3}$	7.61269	1313.59641	3696.9	15	7.423	10.0 ± 0.2	9.2 ± 0.6	1.264 ± 0.067	4.50 ± 0.39
$4_{0,4}-5_{3,3}$	7.61335	1313.48301	2614.9	9	0.2621	8.5 ± 0.1	8.3 ± 0.3	2.504 ± 0.061	227.16 ± 9.05
$7_{5,2}-8_{6,3}$	7.61872	1312.55566	3919.5	45	10.09	9.8 ± 0.2	11.8 ± 0.5	2.202 ± 0.070	7.40 ± 0.40
$7_{5,3}-8_{6,2}$	7.61963	1312.39954	3919.3	15	10.09	8.7 ± 0.3	9.7 ± 0.8	0.928 ± 0.056	2.56 ± 0.26
$7_{3,5}-8_{4,4}$	7.64421	1308.17886	3510.6	15	4.296	9.8 ± 0.2	11.5 ± 0.4	1.707 ± 0.053	13.05 ± 0.65
$3_{1,2}-4_{4,1}$	7.78631	1284.30575	2550.1	21	0.01255	8.3 ± 0.3	13.7 ± 0.9	0.651 ± 0.031	2032.20 ± 163.19
$5_{0,5}-6_{3,4}$	7.86295	1271.78782	2763.6	33	0.2945	8.7 ± 0.1	10.2 ± 0.4	2.936 ± 0.080	291.17 ± 13.26
$6_{1,6}-7_{2,5}$	7.93435	1260.34347	2939.1	39	0.4262	8.8 ± 0.2	10.3 ± 0.7	1.532 ± 0.073	105.75 ± 8.48
					ν SiO				($\times 10^9$cm^{-2})
R27	7.89890	1265.998663	2608.4	57	3.2883	11.1 ± 0.5	12.3 ± 1.8	0.511 ± 0.053	5.47 ± 0.96
R25	7.91344	1263.672931	2494.8	53	3.288	10.1 ± 0.6	13.8 ± 2.1	0.532 ± 0.059	6.41 ± 1.22
R24	7.92083	1262.494014	2441.1	51	3.2874	11.9 ± 0.4	14.8 ± 1.4	0.585 ± 0.041	7.57 ± 0.90
R23	7.92830	1261.304429	2389.5	49	3.2865	10.4 ± 0.3	13.6 ± 1.1	0.712 ± 0.042	8.42 ± 0.82
R22	7.93585	1260.104199	2339.9	47	3.2853	12.1 ± 0.4	10.6 ± 1.6	0.831 ± 0.088	7.71 ± 1.44
R21	7.94348	1258.89335	2292.4	45	3.2837	9.3 ± 0.5	12.8 ± 1.5	0.733 ± 0.064	8.19 ± 1.21
R20	7.95120	1257.671903	2246.9	43	3.2817	10.2 ± 0.4	14.9 ± 1.4	0.771 ± 0.050	10.00 ± 1.12
R18	7.96687	1255.197323	2162.1	39	3.2762	9.2 ± 0.2	12.8 ± 0.8	0.958 ± 0.042	10.71 ± 0.80
R17	7.97484	1253.944235	2122.9	37	3.2727	7.9 ± 0.4	13.4 ± 1.2	0.875 ± 0.048	10.27 ± 1.10
R16	7.98288	1252.680647	2085.6	35	3.2685	10.1 ± 0.4	17.1 ± 2.3	0.942 ± 0.100	14.12 ± 2.42
R15	7.99101	1251.406585	2050.5	33	3.2636	9.0 ± 0.2	13.8 ± 0.6	1.175 ± 0.042	14.27 ± 0.80
R14	7.99922	1250.12207	2017.4	31	3.2578	6.7 ± 0.4	13.3 ± 1.8	1.105 ± 0.105	12.94 ± 2.15
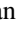
Note. Wavelength and wavenumber are the rest value for each transition, E_u is the energy level of the lower state, k_B is the Boltzmann constant, g_u is the upper statistical weight, A is the Einstein coefficient, $v_{\rm LSR}$ is the observed local standard of rest velocity, $v_{\rm FWHM}$ is the observed FWHM, $S_{\rm Jy} \times S_{\nu 0}$ is the amplitude in units of janskys per arcsecond^2, and N_u is the observed column density of the transition as calculated in Equation (7). Superscripts in the final column for H$_2$ refer to which velocity component the transition is likely associated with: ^{b}blue clump and ^{r}red clump. Data in the first six columns are from the HITRAN database (Gordon et al. 2017) for H$_2$ and H$_2$O, and from the ExoMol database for SiO (Tennyson & Yurchenko 2012).

Table 13
Observed Transitions and Inferred Parameters for Atomic Forbidden Transitions

Position	Wavelength (μm)	Wavenumber (cm^{-1})	A ($\times 10^{-3}$ s^{-1})	v_{LSR} (km s^{-1})	v_{FWHM} (km s^{-1})	Emission Peak (Jy arcsec^{-2})	N_u ($\times 10^{14}$ cm^{-2})
			[Ne II]				
On	12.81355 ± 0.00002	780.42397 ± 0.00122	8.59	-3.44 ± 0.06	11.81 ± 0.16	60.247 ± 0.653	2.37 ± 0.02
Off				-5.06 ± 0.04	8.93 ± 0.08	53.749 ± 0.441	1.60 ± 0.01
			[S III]				
On	18.713 ± 0.001	534.388 ± 0.029	2.06	-6.48 ± 0.02	14.12 ± 0.05	151.694 ± 0.464	29.74 ± 0.07
Off				-7.75 ± 0.04	10.89 ± 0.10	120.605 ± 0.855	18.24 ± 0.10
Off: Wing				-19.65 ± 0.05	9.53 ± 0.14	18.087 ± 0.164	2.39 ± 0.02
			[S I]				
On	25.245 ± 0.001	396.118 ± 0.016	1.40	33.18 ± 0.46	12.18 ± 1.00	3.576 ± 0.203	0.89 ± 0.04
Off				50.89 ± 0.17	11.24 ± 0.18	16.340 ± 0.203	3.75 ± 0.04
			[Fe II]				
Off	25.98839 ± 0.00002	384.78721 ± 0.00030	2.13	51.53 ± 0.05	5.41 ± 0.20	15.599 ± 0.362	1.13 ± 0.02

Note. Position is the position of the line as explained in Section 3.4 (on-source, off-source, and extended blue wing of off-source), wavelength and wavenumber are the rest value for each transition, A is the Einstein coefficient, v_{LSR} is the observed local standard of rest velocity, v_{FWHM} is the observed FWHM, emission peak is the amplitude in units of janskys per arcsecond^2, and N_u is the observed column density of the transition. Wavelength, wavenumber, and A are from the National Institute of Standards and Technology Atomic Spectra Database (NIST ASD) (Kramida et al. 2021). The v_{LSR} errors are statistical only, and do not include the uncertainties in the rest wavelength.

ORCID iDs

Sarah Nickerson https://orcid.org/0000-0002-7489-3142
Naseem Rangwala https://orcid.org/0000-0001-9920-7391
Sean W. J. Colgan https://orcid.org/0000-0001-6275-7437
Curtis DeWitt https://orcid.org/0000-0002-6528-3836
Jose S. Monzon https://orcid.org/0000-0002-9986-4604
Xinchuan Huang https://orcid.org/0000-0003-2458-5050
Kinsuk Acharyya https://orcid.org/0000-0002-0603-8777
Maria N. Drozdovskaya https://orcid.org/0000-0001-7479-4948
Ryan C. Fortenberry https://orcid.org/0000-0003-4716-8225
Eric Herbst https://orcid.org/0000-0002-4649-2536
Timothy J. Lee https://orcid.org/0000-0002-2598-2237

References

Acharyya, K., & Herbst, E. 2018, ApJ, 859, 51
Adams, F. C. 2010, ARA&A, 48, 47
Aikawa, Y., Wakelam, V., Garrod, R. T., & Herbst, E. 2008, ApJ, 674, 993
Allers, K. N., Jaffe, D. T., Lacy, J. H., Draine, B. T., & Richter, M. J. 2005, ApJ, 630, 368
Bachiller, R., & Gutiérrez, M. P. 1997, ApJ, 487, L93
Bally, J., Cunningham, N. J., Moeckel, N., et al. 2011, ApJ, 727, 113
Bally, J., Ginsburg, A., Arce, H., et al. 2017, ApJ, 837, 60
Bally, J., Ginsburg, A., Silvia, D., & Youngblood, A. 2015, A&A, 579, A130
Barber, R. J., Strange, J. K., Hill, C., et al. 2013, MNRAS, 437, 1828
Barentine, J. C., & Lacy, J. H. 2012, ApJ, 757, 111
Barr, A. G., Boogert, A., DeWitt, C. N., et al. 2018, ApJL, 868, L2
Barr, A. G., Boogert, A., DeWitt, C. N., et al. 2020, ApJ, 900, 104
Barr, A. G., Boogert, A., Li, J., et al. 2022, ApJ, 935, 165
Beck, S. C. 1984, ApJ, 281, 205
Becklin, E. E., & Neugebauer, G. 1967, ApJ, 147, 799
Beckwith, S., Persson, S. E., Neugebauer, G., & Becklin, E. E. 1978, ApJ, 223, 464
Beltrán, M. T., & Rivilla, V. M. 2018, in ASP Conf. Ser. 517, Science with a Next Generation Very Large Array, ed. E. Murphy (San Francisco, CA: ASP), 249
Beuther, H., Linz, H., Bik, A., Goto, M., & Henning, T. 2010, A&A, 512, A29
Bilalbegović, G., & Baranović, G. 2015, MNRAS, 446, 3118
Blake, G. A., Mundy, L. G., Carlstrom, J. E., et al. 1996, ApJL, 472, L49
Blake, G. A., Sutton, E. C., Masson, C. R., & Phillips, T. G. 1987, ApJ, 315, 612

Bolatto, A. D., Wolfire, M., & Leroy, A. K. 2013, ARA&A, 51, 207
Boogert, A. C., Helmich, F. P., Dishoeck, E. F. V., et al. 1998, A&A, 336, 352
Boogert, A. C., Schutte, W. A., Helmich, F. P., Tielens, A. G., & Wooden, D. H. 1997, A&A, 317, 929
Boogert, A. C., Schutte, W. A., Tielens, A. G., et al. 1996, A&A, 315, L377
Boogert, A. C. A., Blake, G. A., & Oberg, K. 2004, ApJ, 615, 344
Boonman, A. M., van Dishoeck, E. F., Lahuis, F., et al. 2003, A&A, 399, 1047
Brand, P. W. J. L., Toner, M. P., Geballe, T. R., & Webster, A. S. 1989, MNRAS, 237, 1009
Burkhardt, A. M., Shingledecker, C. N., Gal, R. L., et al. 2019, ApJ, 881, 32
Burton, M. G., & Haas, M. R. 1997, A&A, 327, 309
Campbell, B., & Persson, S. E. 1988, AJ, 95, 1185
Capps, R. W., Gillett, F. C., & Knacke, R. F. 1987, ApJ, 226, 863
Carr, J. S., II, Lacy, N. J. E., & Zhou, S, J. H. 1995, ApJ, 450, 667
Cesaroni, R. 2005, in IAU Symp. 227, Massive Star Birth: A Crossroads of Astrophysics, ed. R. Cesaroni et al. (Cambridge: Cambridge Univ. Press), 59
Charnley, S. B. 1997, ApJ, 481, 396
Churchwell, E., Wood, D. O. S., Felli, M., & Massi, M. 1987, ApJ, 321, 516
Clarke, M., Vacca, W. D., & Shuping, R. Y. 2015, in ASP Conf. Ser. 495, Astronomical Data Analysis Software an Systems XXIV, ed. A. R. Taylor & E. Rosolowsky (San Francisco, CA: ASP), 355
Comito, L., Sipilä, O., Roueff, E., Caselli, P., & Fontani, F. 2020, A&A, 640, A51
Comito, C., Schilke, P., Phillips, T. G., et al. 2005, ApJS, 156, 127
Crockett, N. R., Bergin, E. A., Neill, J. L., et al. 2014, ApJ, 787, 112
Daniel, F., Gérin, M., Roueff, E., et al. 2013, A&A, 560, A3
de Vicente, P., Martín-Pintado, J., Neri, R., & Rodríguez-Franco, A. 2002, ApJL, 574, L163
des Forets, G. P., Roueff, E., Schilke, P., & Flower, D. R. 1993, MNRAS, 262, 915
Dickens, J. E., & Irvine, W. M. 1999, ApJ, 518, 733
Draine, B. T. 1989, Infrared Spectroscopy om Astronomy, Vol. 290 (Noordwijk: ESA), 93
Dungee, R., Boogert, A., DeWitt, C. N., et al. 2018, ApJL, 868, L10
Esplugues, G. B., Tercero, B., Cernicharo, J., et al. 2013, A&A, 556, A143
Evans, N. J., Lacy, J. H., & Carr, J. S. 1991, ApJ, 383, 674
Favre, C., Despois, D., Brouillet, N., et al. 2011, A&A, 532, A32
Favre, C., Carvajal, M., Field, D., et al. 2014, ApJS, 215, 25
Feng, S., Beuther, H., Henning, T., et al. 2016, A&A, 590, C1
Foreman-Mackey, D., Hogg, D. W., Lang, D., & Goodman, J. 2013, PASP, 125, 306
Friedel, D. N., & Looney, L. W. 2017, ApJ, 154, 152
Gavilan, L., Vidali, G., Lemaire, J. L., et al. 2012, ApJ, 760, 35
Genzel, R., Ho, P. T. P., Bieging, J., & Downes, D. 1982, ApJL, 259, L103
Genzel, R., & Stutzki, J. 1989, ARA&A, 27, 41
Gezari, D. Y. 1992, ApJL, 396, L43

Gnedin, N. Y., & Kravtsov, A. V. 2011, ApJ, 728, 88
Goddi, C., Greenhill, L. J., Humphreys, E. M. L., Chandler, C. J., & Matthews, L. D. 2011, ApJL, 739, L13
Goldsmith, P. F., & Langer, W. D. 1999, ApJ, 517, 209
Gomez, L., RodrIguez, L. F., Loinard, L., et al. 2005, ApJ, 635, 1166
Gong, Y., Henkel, C., Thorwirth, S., et al. 2015, A&A, 581, A48
Gordon, I. E., Rothman, L. S., Hill, C., et al. 2017, JQSRT, 203, 3
de Graauw, T. D., Haser, L. N., Beintema, D. A., et al. 1996, A&A, 315, L49
Greenhill, L. J., Gezari, D. Y., Danchi, W. C., et al. 2004, ApJ, 605, L57
Greenhill, L. J., Gwinn, C. R., Schwartz, C., Moran, J. M., & Diamond, P. J. 1998, Natur, 396, 650
Harris, G. J., Tennyson, J., Kaminsky, B. M., Pavlenko, Y. V., & Jones, H. R. A. 2006, MNRAS, 367, 400
Hartquist, T. W., Oppenheimer, M., & Dalgarno, A. 1980, ApJ, 236, 182
Hasegawa, T. I., Herbst, E., & Leukng, C. M. 1992, ApJS, 82, 167
Hatchell, J., Thompson, M. A., Millar, T. J., & Macdonald, G. H. 1998, A&A, 338, 713
Hermsen, W., Wilson, T. L., Walmsley, C. M., & Henkel, C. 1988, A&A, 201, 285
Herpin, F., Marseille, M., Wakelam, V., Bontemps, S., & Lis, D. C. 2009, A&A, 504, 853
Hirota, T., Kim, M. K., Kurono, Y., & Honma, M. 2015, ApJ, 801, 82
Hirota, T., Machida, M. N., Matsushita, Y., et al. 2017, NatAs, 1, 0146
Ho, P. T. P., Barrett, A. H., Myers, P. C., et al. 1979, ApJ, 234, 912
Ho, P. T. P., & Townes, C. H. 1983, ARA&A, 21, 239
Hunter, J. D. 2007, CSE, 9, 90
Indriolo, N., Tan, J. C., Boogert, A. C. A., et al. 2018, ApJL, 865, L18
Indriolo, N., Neufeld, D. A., Gerin, M., et al. 2015, ApJ, 800, 40
Indriolo, N., Neufeld, D. A., Barr, A. G., et al. 2020, ApJ, 894, 107
Jacquinet-Husson, N., Armante, R., Scott, N. A., et al. 2016, JMoSp, 327, 31
Johansson, L. E. B., Andersson, C., Ellder, J., et al. 1984, A&A, 130, 227
Jørgensen, J. K., Müller, H. S., Calcutt, H., et al. 2018, A&A, 620, A170
Kaufman, M. J., Hollenbach, D. J., & Tielens, A. G. G. M. 1998, ApJ, 497, 276
Keane, J. V., Boonman, A. M. S., Tielens, A. G. G. M., & van Dishoeck, E. F. 2004, A&A, 376, L5
Keto, E., Rawlings, J., & Caselli, P. 2014, MNRAS, 440, 2616
Kim, M. K., Hirota, T., Honma, M., et al. 2008, PASJ, 60, 991
Kleinmann, D. E., & Low, F. J. 1967, ApJ, 149, L1
Knez, C., Lacy, J. H., Evans, N. J., van Dishoeck, E. F., & Richter, M. J. 2009, ApJ, 696, 471
Kochanov, R. V., Gordon, I. E., Rothman, L. S., et al. 2016, JQSRT, 177, 15
Kramida, A., Yuri, R., & Reader, J. 2021, NIST Atomic Spectra Database (ver. 5.9) https://physics.nist.gov/asd
Kurtz, S., Cesaroni, R., Churchwell, E., Hofner, P., & Walmsley, C. M. 2000, in Protostars and Planets IV, ed. V. Mannings, A. P. Boss, & S. S. Russell (Tucson, AZ: Univ. Arizona Press), 299
Lacy, J. H. 2013, ApJ, 765, 130
Lacy, J. H., Carr, J. S., Evans, N. J., II, et al. 1991, APJ, 376, 556
Lacy, J. H., II, , N. J. E., Achtermann, J. M., et al. 1989, ApJL, 342, L43
Lacy, J. H., Richter, M. J., Greathouse, T. K., Jaffe, D. T., & Zhu, Q. 2002, PASP, 114, 153
Lerate, M. R., Barlow, M. J., Swinyard, B. M., et al. 2006, MNRAS, 370, 597
Leroy, A. K., Walter, F., Sandstrom, K., et al. 2013, AJ, 146, 19
Lord, S. D. 1992, A new software tool for computing Earth's atmospheric transmission of near- and far-infrared radiation, NASA Technical Memorandum103957NASA Technical Memorandum
Luo, G., Feng, S., Li, D., et al. 2019, ApJ, 885, 82
Lupi, A., Bovino, S., & Grassi, T. 2021, A&A, 654, L6
Magalhães, V. S., Hily-Blant, P., Faure, A., Hernandez-Vera, M., & Lique, F. 2018, A&A, 615, A52
Markwick, A. J., Millar, T. J., & Charnley, S. B. 2000, ApJ, 535, 256
Menten, K. M., & Reid, M. J. 1995, ApJL, 445, L157
Milam, S. N., Savage, C., Brewster, M. A., Ziurys, L. M., & Wyckoff, S. 2005, ApJ, 634, 1126
Mitchell, G. F., Maillard, J.-P., Allen, M., Beer, R., & Belcourt, K. 1990, ApJ, 363, 554
Mookerjea, B., Casper, E., Mundy, L. G., & Looney, L. W. 2007, ApJ, 659, 447
Murata, Y., Kawabe, R., Ishiguro, M., et al. 1990, ApJ, 359, 125
Nickerson, S., Rangwala, N., Colgan, S., et al. 2021, ApJ, 907, 51
Nissen, H. D., Cunningham, N. J., Gustafsson, M., et al. 2012, A&A, 540, A119
Nissen, H. D., Gustafsson, M., Lemaire, J. L., et al. 2007, A&A, 466, 949
O'Dell, C. R., Abel, N. P., & Ferland, G. J. 2020, ApJ, 891, 46

O'Dell, C. R., Kollatschny, W., & Ferland, G. J. 2017, ApJ, 837, 151
Okumura, S.-i., Yamashita, T., Sako, S., et al. 2011, PASJ, 63, 823
Olofsson, A. O., Persson, C. M., Koning, N., et al. 2007, A&A, 476, 791
Orozco-Aguilera, M. T., Zapata, L. A., Hirota, T., Qin, S.-L., & Masqué, J. M. 2017, ApJ, 847, 66
Öberg, K., Boogert, A. C. A., Pontoppidan, K., et al. 2008, ApJ, 678, 1032
Pagani, L., Lesaffre, P., Jorfi, M., et al. 2013, A&A, 551, A38
Parmar, P. S., Lacy, J. H., & Achtermann, J. M. 1994, ApJ, 430, 786
Peng, Y., Rivilla, V. M., Zhang, L., Ge, J. X., & Zhou, B. 2019, ApJ, 871, 251
Persson, C. M., Olofsson, A. O. H., Koning, N., et al. 2007, A&A, 476, 807
Plambeck, R. L., Wright, M. C. H., Friedel, D. N., et al. 2009, ApJL, 704, L25
Plume, R., Bergin, E. A., Phillips, T. G., et al. 2012, ApJ, 744, 28
Price-Whelan, A. M., Sipőcz, B. M., Gunther, H. M., et al. 2018, ApJ, 156, 123
Qasim, D., Fedoseev, G., Chuang, K.-J., et al. 2020, NatAs, 4, 781
Qin, S.-L., Liu, T., Liu, X., et al. 2022, MNRAS, 511, 3463
Rangwala, N., Colgan, S. W. J., Gal, R. L., et al. 2018, ApJ, 856, 9
Richter, M. J., DeWitt, C. N., McKelvey, M., et al. 2018, JAI, 7, 1840013
Rieke, G. H., Low, F. J., & Kleinmann, D. E. 1973, ApJL, 186, L7
Rizzo, J. R., Tercero, B., & Cernicharo, J. 2017, A&A, 605, A76
Robitaille, T. P., Tollerud, E. J., Greenfield, P., et al. 2013, A&A, 558, A33
Rosenthal, D., Bertoldi, F., & Drapatz, S. 2000, A&A, 356, 705
Rubin, R. H., Simpson, J. P., O?Dell, C. R., et al. 2011, MNRAS, 410, 1320
Schilke, P., Benford, D. J., Hunter, T. R., Lis, D. C., & Phillips, T. G. 2001, ApJS, 132, 281
Schilke, P., Groesbeck, T. D., Blake, G. A., & Phillips, T. G. 1997, ApJS, 108, 301
Schilke, P., Walmsley, C. M., des Forêts, G. P., et al. 1992, A&A, 256, 595
Scoville, N., Kleinmann, S. G., & Ridgway, S. T. 1983, ApJ, 275, 201
Shuping, R. Y., Morris, M., & Bally, J. 2004, AJ, 128, 363
Simpson, J. P., Colgan, S. W. J., Erickson, E. F., Burton, M. G., & Schultz, A. S. B. 2006, ApJ, 642, 339
Sutton, E. C., Peng, R., Danchi, W. C., et al. 1995, ApJS, 97, 455
Takahashi, J. 2001, ApJ, 561, 254
Tennyson, J., & Yurchenko, S. N. 2012, MNRAS, 425, 21
Tercero, B., Cernicharo, J., Pardo, J. R., & Goicoechea, J. R. 2010, A&A, 517, A96
Tercero, B., Vincent, L., Cernicharo, J., Viti, S., & Marcelino, N. 2011, A&A, 528, A26
Tieftrunk, A., des Forêts, G. P., Schilke, P., & Walmsley, C. M. 1994, A&A, 289, 579
Tielens, A. G. G. M., & Whittet, D. C. B. 1997, in IAU Symp. 178, Molecules in astrophysics: probes & processes, ed. E. F. van Dishoeck (Cambridge: Cambridge Univ. Press), 45
Troscompt, N., Faure, A., Maret, S., et al. 2009, A&A, 506, 1243
van der Tak, F. F., Boonman, A. M., Braakman, R., & Dishoeck, E. F. V. 2003, A&A, 412, 133
van der Tak, F. F. S. 2004, in IAU Symp. 221, Star Formation at High Angular Resolution, ed. M. G. Burton, R. Jayawardhana, & T. L. Bourke (Cambridge: Cambridge Univ. Press), 59
van der Walt, S., Colbert, S. C., & Varoquaux, G. 2011, CSE, 13, 22
van Dishoeck, E. F., & Blake, G. A. 1998, ARA&A, 36, 317
van Dishoeck, E. F., Wright, C. M., Helmich, F. P., et al. 1998, ApJ, 502, L173
Vidal, T. H. G., & Wakelam, V. 2018, MNRAS, 474, 5575
Virtanen, P., Gommers, R., Oliphant, T. E., et al. 2020, NatMe, 17, 261
Wakelam, V., Caselli, P., Ceccarelli, C., Herbst, E., & Castets, A. 2004, A&A, 422, 159
Wakelam, V., Bron, E., Cazaux, S., et al. 2017, MolAs, 9, 1
Wilkins, O. H., Carroll, P. B., & Blake, G. A. 2022, ApJ, 924, 4
Wilson, T. L., Gaume, R. A., Gensheimer, P., & Johnston, K. L. 2000, ApJ, 538, 665
Wilson, T. L., Henkel, C., Huettemesiter, S., et al. 1993, A&A, 276, L29
Woods, P. M., Occhiogrosso, A., Viti, S., et al. 2015, MNRAS, 450, 1256
Wright, C. M., VanDishoeck, E. F., Black, J. H., et al. 2000, A&A, 358, 689
Wright, M., Plambeck, R., Hirota, T., et al. 2020, ApJ, 889, 155
Wright, M., Bally, J., Hirota, T., et al. 2022, ApJ, 924, 107
Wright, M. C. H., & Plambeck, R. L. 2017, ApJ, 843, 83
Wright, M. C. H., Plambeck, R. L., & Wilner, D. J. 1996, ApJ, 469, 216
Wynn-Williams, C. G., Genzel, R., Becklin, E. E., & Downes, D. 1984, ApJ, 281, 172
Xue, M., Jiang, B. W., Gao, J., et al. 2016, ApJS, 224, 23
Young, E. T., Becklin, E. E., Marcum, P. M., et al. 2012, ApJL, 749, 17
Zapata, L. A., Rodríguez, L. F., Schmid-Burgk, J., et al. 2012, ApJL, 754, L17
Zapata, L. A., Schmid-Burgk, J., & Menten, K. M. 2011, A&A, 529, A24
Ziurys, L. M., Schmidt, D. R., & Woolf, N. J. 2020, ApJL, 900, L31